LHCb 2006-006
27 January 2006

Test-beam Results from a RICH Detector Prototype Using Aerogel Radiator and Pixel Hybrid Photon Detectors

Gianluca Aglieri Rinella[1], Thierry Gys[1] Ann Van Lysebetten[1], Didier Piedigrossi[1], Ken Wyllie[1], Tito Bellunato[2] Marta Calvi[2], Clara Matteuzzi[2], Marco Musy[2], Davide Perego[2], Laura Somerville[3], Charlotte Newby[3], Sajan Easo[4], Steve Wotton[5]

([1]) *CERN*
([2]) *University of Milano-Bicocca and INFN, Milano, Italy*
([3]) *University of Oxford*
([4]) *Rutherford Laboratory*
([5]) *University of Cambridge*

Abstract

A test-beam study was performed at CERN with a Ring Imaging Cherenkov (RICH) prototype using three pixel Hybrid Photon Detectors. Results on the photon yield and Cherenkov angle resolution are presented here, for the Aerogel radiator and also for reference runs taken with Nitrogen radiator.

1 Introduction

The LHCb RICH aerogel test which took place in October 2003 had a twofold purpose: to evaluate the performance of thick silica aerogel tiles as Cherenkov radiators, in terms of photon yield and Cherenkov angle resolution, and to test the performance of the latest LHCb Hybrid Photon Detectors (HPD) prototypes in a Ring Imaging Cherenkov detector with the aerogel radiator.

2 The experimental setup

A light-tight vessel, shown schematically in Figure 1, contained the aerogel tiles, a spherical mirror with radius of curvature R=949 cm and three HPDs. Nitrogen was flushed through the vessel to protect the hygroscopic aerogel from humidity. The vessel was located in the T9 beam test facility at the CERN PS accelerator complex. From the primary proton beam of 24 GeV/c the secondary beams can be selected in momentum and charge. The beamline can give a pure π^- beam, or a mixture of π^+ and p. Data were taken with both positive and negative particles with beam momentum of 10 GeV/c. The particles crossing the silica aerogel tile generated Cherenkov photons which were reflected off a spherical mirror and focused onto the photon detector plane. In the normal data-taking configuration, the Cherenkov light from the N_2 between the aerogel and the mirror was focused in the central region not covered by the detectors. Data were taken also using N_2 only as radiator medium (without aerogel) for calibration purposes. The mirror was in this case re-aligned to focus the corresponding Cherenkov rings onto each of the three photon detectors in turn, and the ring was fully contained on a single HPD, given the smaller Cherenkov angle.

The entire vessel could be moved in the three directions by an adjustable support. The displacement of the vessel relative to the beam allowed the scanning of different aerogel regions, with the particles crossing the tiles at various positions. The effects due to the surfaces between the adjacent tiles were also investigated, with the beam crossing parallel to the boundary between tiles. Figure 2 shows a schematic description of the full experimental setup. The trigger signal was provided by the coincidence of a set of scintillators located on the beam line. Two scintillators of 1×1 cm^2, located $\sim$8 m apart, limited the beam divergence to $\sim$1.5 mrad. Three pixel silicon detector planes were installed in the beam line for tracking the particles. The data obtained by the tracking detector have been used for determining the particle trajectory event by event.

2.1 The Photodetectors

Three pixel Hybrid Photon Detectors [1] (named HPD0, HPD1, HPD2 here on) were used as photon detectors. They were located on the upper side of the vessel, at the vertices of an equilateral triangle, as shown in Figure 1.

The HPD, shown in Figures 3 and 4, is a vacuum tube in the external dimension of 80 mm diameter and 115 mm height. A S20 blue-enhanced multi-alkali photo-cathode is deposited on the internal surface of the quartz entrance window, the thickness of which is 7 mm. Figure 5 shows the quantum efficiency curves of the three HPDs used, as measured at their production. The three curves show maxima in the range 23-29% around 270 nm, and a second typical peak at 440 nm, where values around 19% are measured.

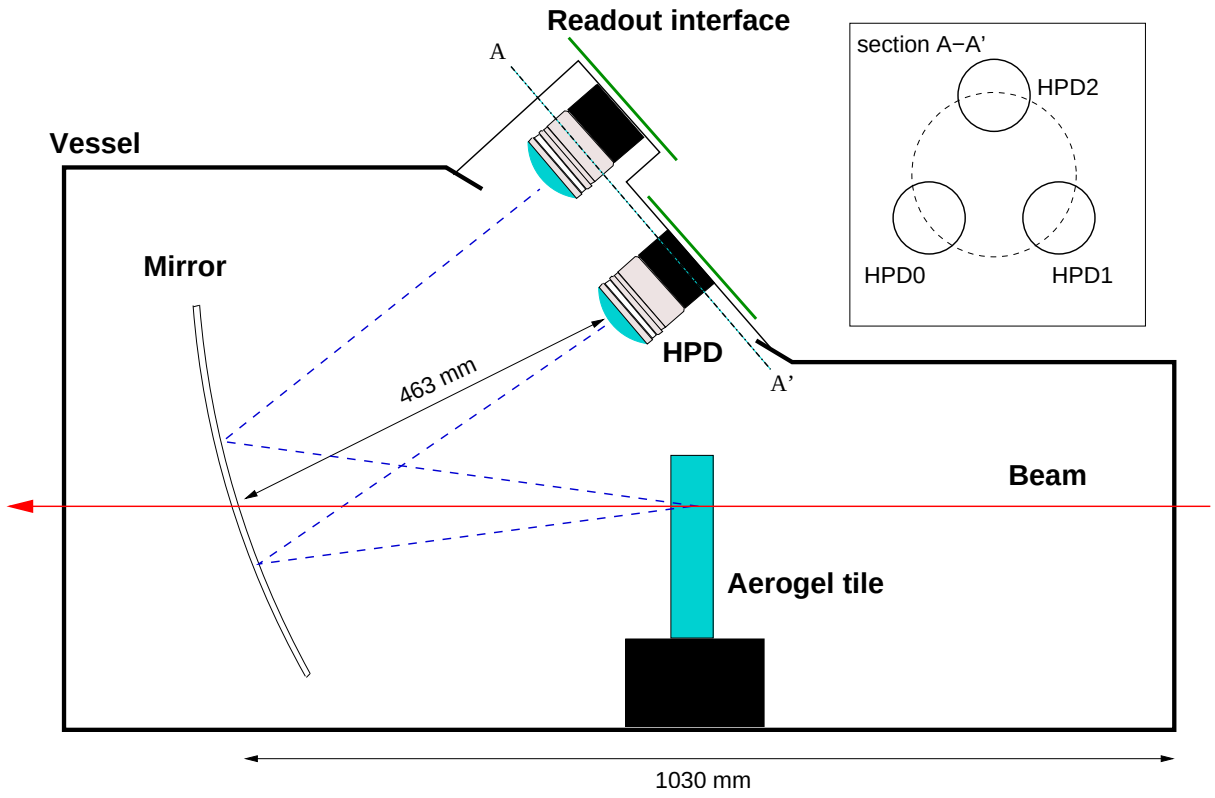

Figure 1: The light-tight vessel.

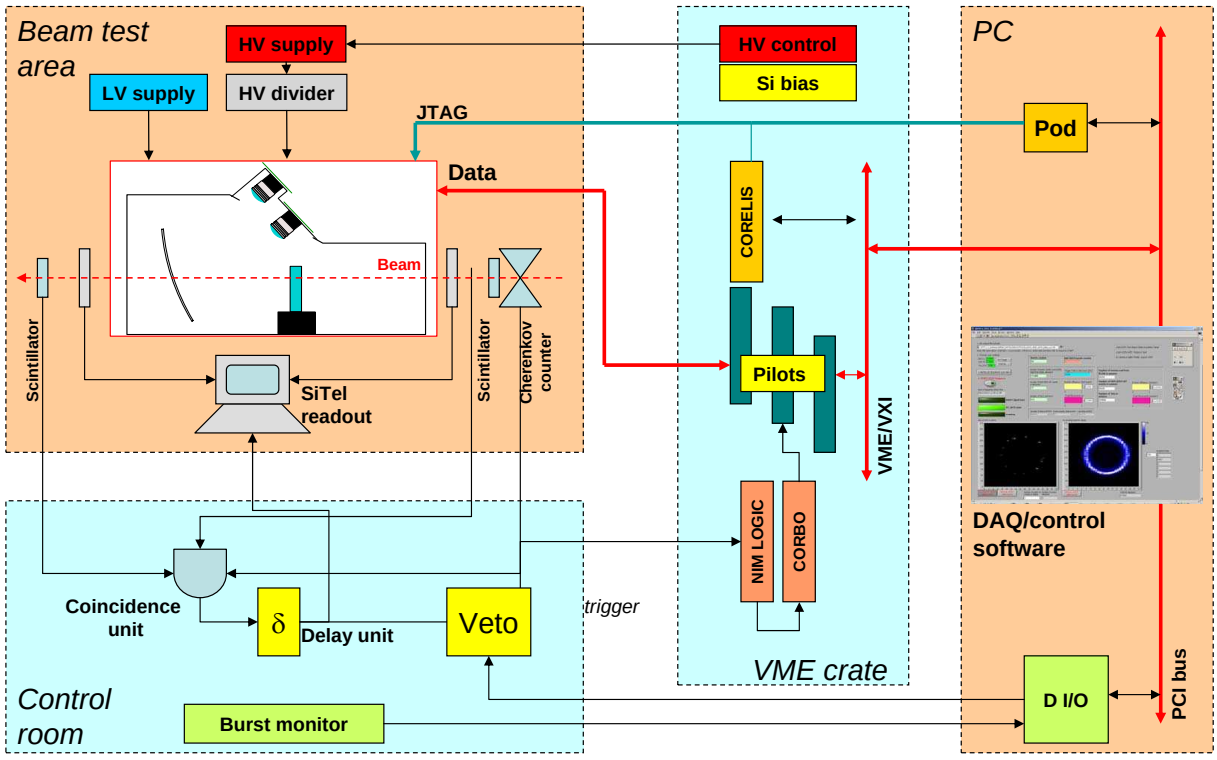

Figure 2: Schematic drawing of the October 2003 LHCb-RICH beam test setup.

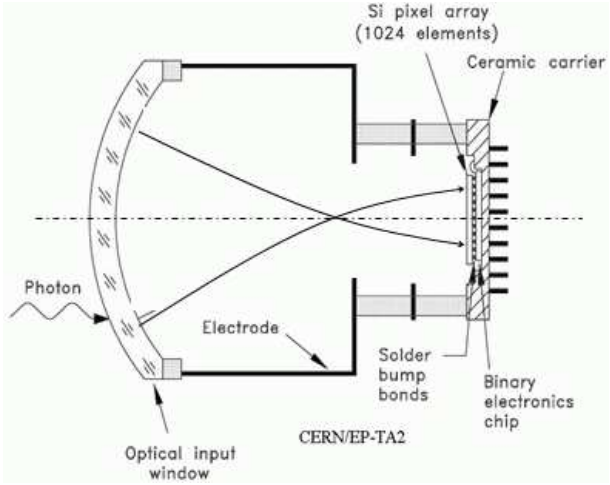

Figure 3: Schematic principle of the HPD.

Figure 4: The pixel Hybrid Photon Detector.

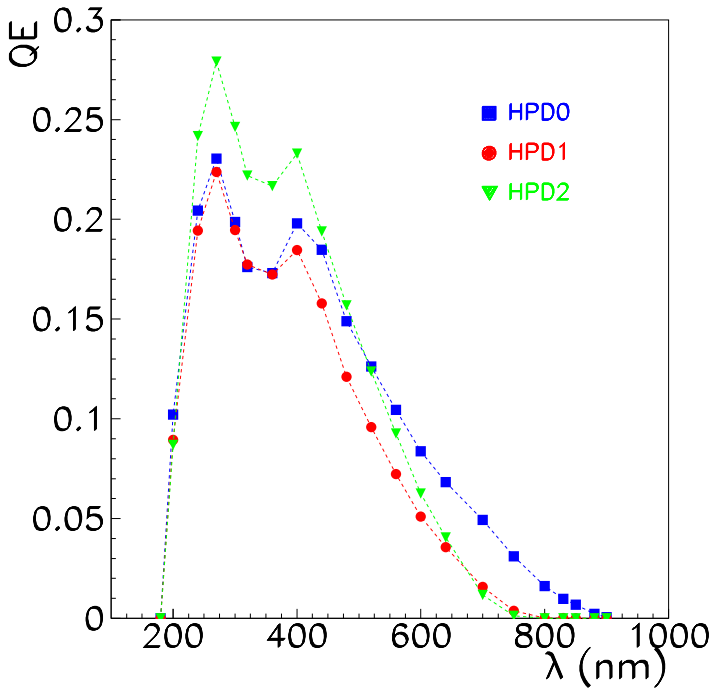

Figure 5: Quantum efficiency curves for the three HPDs used in the beam test.

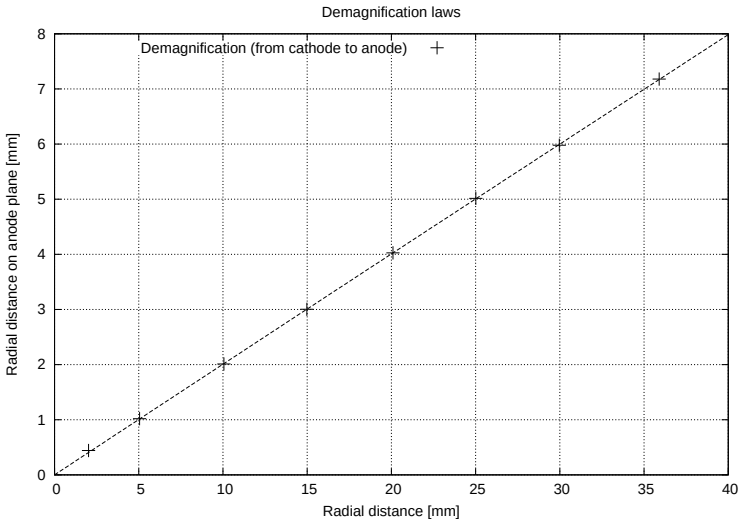

Figure 6: Demagnification law. Calculated points and linear fit are shown.

The photo-electrons emitted from the cathode are accelerated toward the anode in a cross-focusing electron optics system. The electron optics has three electrodes to be biased with a set of three high voltages, obtained from the cathode voltage supply by an external resistive voltage divider. The nominal cathode operating voltage is 20 kV but during test-beam running the HPDs were biased at 18 kV due to limitations of the HV insulation in the setup. The demagnification law can be defined as the radial distance of the photo-electron hit on the anode as a function of the radial distance of the emission point on the cathode. The setup lacked accurate monitoring of the electrode high voltages, the ratios of which influence the demagnification law. The demagnification law used in the data analysis is shown in Figure 6. It corresponds to the simplest linear relationship $R_{cathode} = -5 \times R_{anode}$. It has been evaluated by numerical simulations of the electron trajectories, tuning the voltages applied in such a way to reproduce the features recorded in the data runs. This was achieved for a cathode to focusing electrode voltage difference of 220 V.

The anode assembly is fully encapsulated in the vacuum envelope (Figure 3). HPD0 and HPD1 contain final prototypes of the LHCb HPD anode assembly. The assembly consists of a hybrid pixel detector with a pixelated silicon sensor bump-bonded onto a CMOS readout chip, LHCBPIX1 [2]. The anode has 32×256 pixels of 500×62.5 μm^2, corresponding to an effective pixel size of 2.5×0.31 mm^2 on the entrance window. The pixels of the silicon detector are connected via the bump-bonds to the LHCBPIX1 chip channels, each of which contains a full analogue front-end amplification and discrimination section, followed by a 40 MHz digital section. HPD2 is an older prototype featuring a different anode assembly, a common development of the ALICE and LHCb collaborations. The dimensions of the hybrid pixel detector are smaller in this case. The sensor also has 32×256 pixels but they are smaller in size: 400×50 μm^2. The CMOS readout chip onto which the sensor is bump-bonded is the ALICE1LHCB chip, from which the LHCBPIX1 was further developed.

The HPD has an excellent S/N ratio performance. The binary data are read out via 32 signal lines fed through the anode carrier. The hybrid technology and on-chip discrimination on each channel provide efficient single photon detection capability with total rejection of electronic noise.

The photo-electron hitting the silicon sensor releases its energy generating electron-hole pairs. The charge signal is integrated, amplified and then discriminated to give a pixel hit. The detection efficiency is the conditional probability of detecting a pixel hit given that a photo-electron hit the detector. It is strongly dependent both on the photo-electron energy, i.e. on the high voltage applied and on the discriminator threshold setting. Even well above the HV threshold, the detection efficiency is less than 100% because of inefficiencies in charge generation and collection, due to back-scattering of the photo-electrons and charge sharing among adjacent pixels. Measurements in a dedicated set-up [3] determined a detection efficiency of 82% operating at 18 kV and at the chosen threshold.

The low and high voltage supplies were installed in the experimental area and could be remotely controlled from the control room. They were needed for biasing the HPD chip, the readout electronics, the silicon sensor (80 V) and the cathode resistive divider chain (18-20 kV). Hence the detection efficiency of the HPDs could be controlled through varying the tube HV.

A custom data acquisition and control software was written for the experimental set-

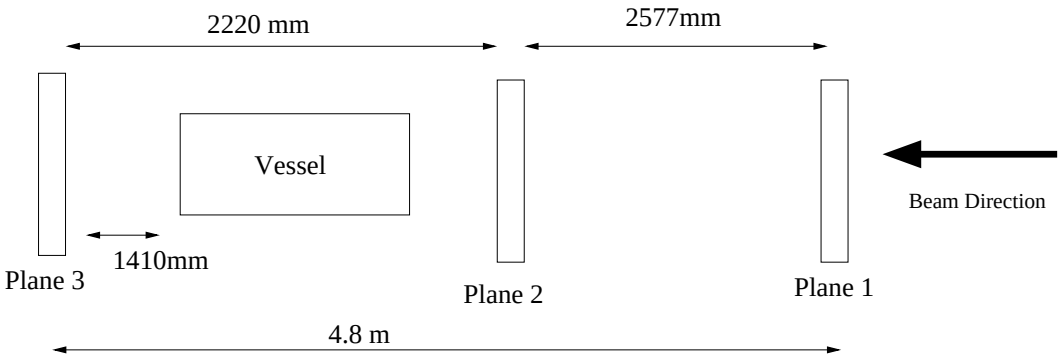

Figure 7: Schematic of the position of the three silicon telescope planes.

up, based on LabView. A control system was arranged to allow the simultaneous control of the three HPD chips and the respective biasing boards.The biasing boards provided the HPD chips with LV biases and voltage references.

The readout of the HPDs binary data was done through three PILOT VME boards, driving the HPD chips at 10 MHz. The signals were driven over the ∼20 m between the beam area and the readout station. The data were read out during a beam spill, buffered in the memory of the PILOT boards and then transferred to the PC for recording during the idle time between consecutive beam spills.

During the beam spill a readout rate of few kHz could be achieved. It was limited to a lower value when using the silicon telescope tracker, in its turn synchronized with the readout of the HPDs. The data readout from the HPD chip formed a binary map of the hits on the 32×256 pixels. The hits were also displayed on three histograms on the PC readout software. Calculation in real time of some quantitative figures from the data, for example event and pixel occupancy, allowed the software to act as an on-line monitor during data acquisition.

2.2 The Beam Monitor

The silicon telescope was used in the test-beam to provide an event-by-event track direction for the Cherenkov angle reconstruction and to measure the beam divergence. It consisted of three planes of silicon pixel detectors, each plane had 22x22 pixels, and each pixel was 1.3 x 1.3 mm^2. Two planes were placed upstream of the vessel containing the aerogel and detector system, the third was downstream, as shown in Figure 7. The first and third plane were separated by about 4.8 meters. A coordinate system was defined with the Z axis along the beam direction and the Y axis vertical, pointing upward.

Each pixel hit was recorded and converted to a digital signal using a 10-bit ADC. Figure 8 shows the ADC charge for a typical run. The noise pedestal towards low ADC values and a saturation effect towards higher ADC values can be clearly seen. These features were removed by a cut on the ADC charge between 125 and 770. To take into account the effect of charge sharing between pixels, a cluster finding algorithm was applied to the data. About 2.5% of the clusters were double hits and less than 1% triple hits. When a cluster was found, a center-of-gravity calculation was carried out to produce a single hit. A minimum total ADC charge of 300 was required for each cluster and events with clusters made of more than 4 hits were rejected. Events were selected where each

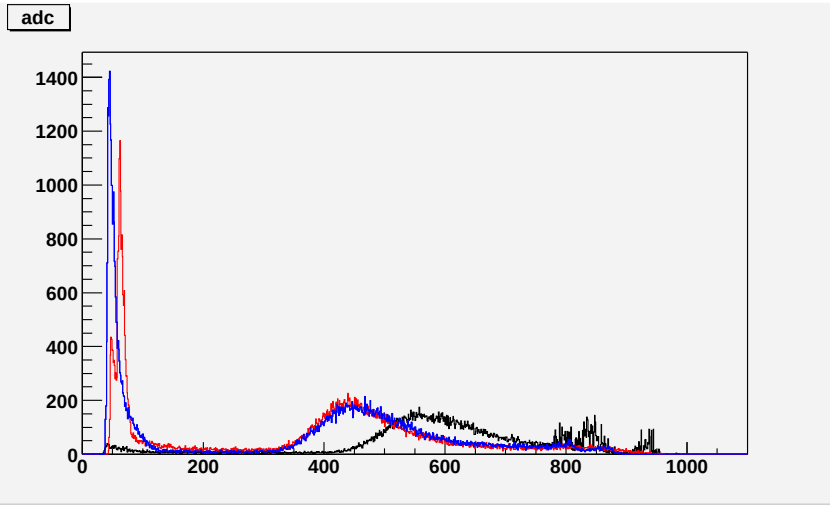

Figure 8: ADC counts for the three silicon plane detectors for a typical run.

of the three silicon telescope planes had exactly one hit. About 65% of the events passed the cuts, consistently for all runs.

The hit density of selected events in the three silicon telescope planes is shown in Figure 9 and was used to align the system. The recorded beam profile was determined by the smaller of the two scintillation counters that triggered the readout. Plane 3 was at the limits of its acceptance. For every event the hits in each plane were fitted with a least squares linear fit in the XZ and YZ planes independently. The residual between the fitted coordinate and the actual hit coordinate was minimized to find the best alignment. The central position determined in each silicon telescope plane defined the nominal beam direction (0,0,1). The beam divergence for the negative beam was found to be 1.6 mrad in X and 0.7 mrad in Y. The contribution to the beam divergence from pixelization is ∼0.05 mrad. Figure 10 shows the divergence of the tracks fitted through the silicon telescope .

2.3 Aerogel Radiator

Aerogel is a low density material made of SiO_2, with small contamination of water and ethanol. Charged particles having β=1 produce Cherenkov photons at an angle of 242 mrad with respect to the particle direction in the aerogel with nominal refractive index n=1.03.

In the test presented in this paper, 4 tiles of about 10x10x4 cm^3 of hygroscopic aerogel were used. They have been produced at the Boreskov Institute of Catalysis in Novosibirsk [4]. They were mounted to form a wall of 2×2 tiles, closely packed, as shown in Figure 11.

An important optical requirement for a Cherenkov radiator is that it should not scatter the produced photons. Any angular dispersion caused by the radiator medium will reduce the precision on the Cherenkov emission angle. The light transmission T at wavelength λ through a sample of thickness L is well described by the expression [5]

$$T = A \cdot e^{-CL/\lambda^4} \tag{1}$$

where C is the clarity coefficient and A is the transmission in the high-λ region.

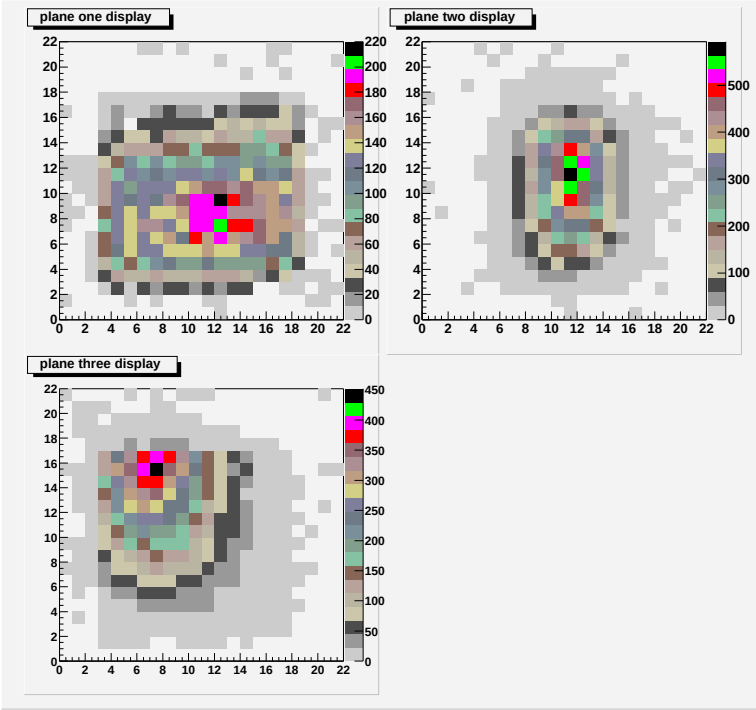

Figure 9: Hit density in the three planes of the silicon telescope, for a typical run, after cuts.

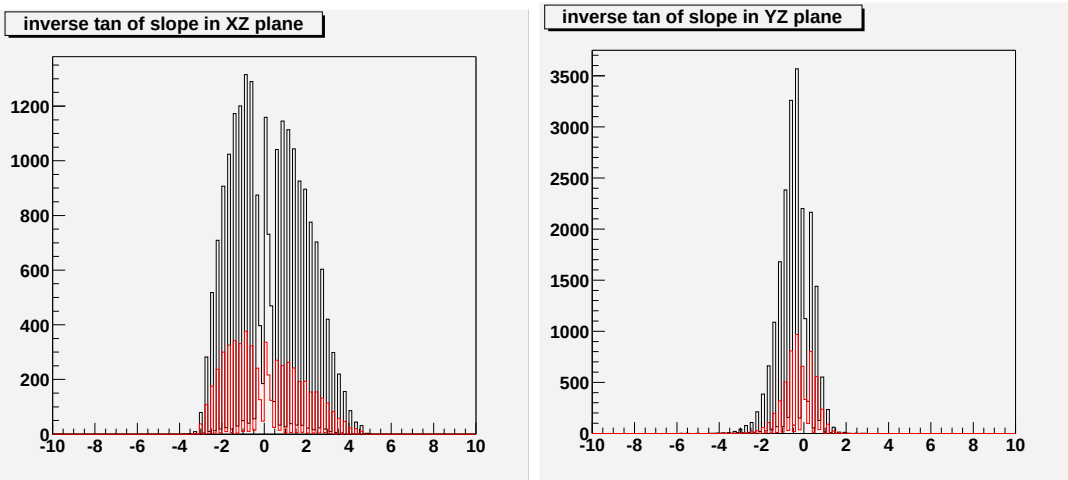

Figure 10: Slope (mrad) of the tracks fitted through the silicon telescope hits, in the XZ and YZ planes. Indicated in red are the subset of events where the track passed through the central region of plane 2.

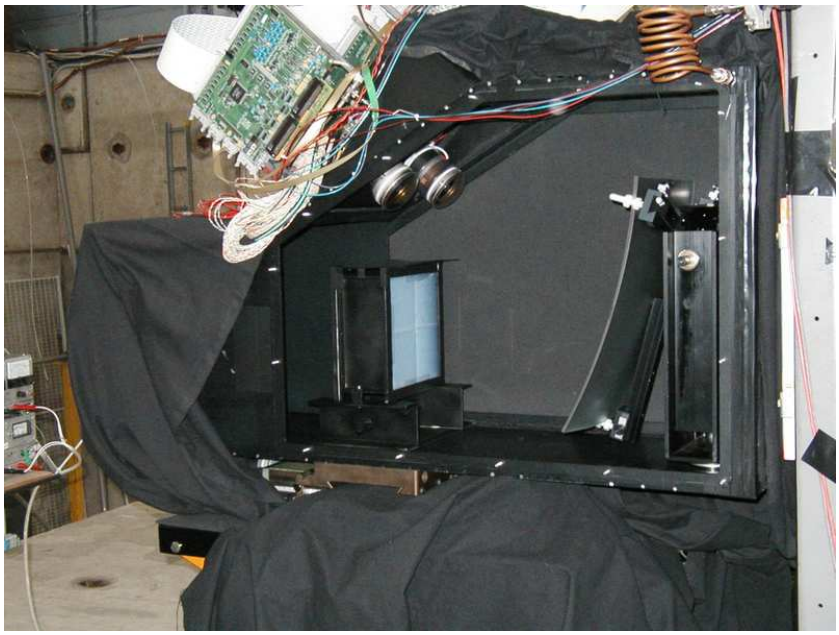

Figure 11: The vessel containing the aerogel wall, the mirror and the three HPDs.

The optical properties of these aerogel samples have been determined by measuring the light transmission as a function of wavelength. The C and A coefficients were determined, fitting equation (1). The properties of the four tiles, as measured before the test, are reported in Table 1.

Tile	1	2	3	4
thickness	4.4 cm	4.2 cm	4.4 cm	4.2 cm
n	1.0286	1.0292	1.0272	1.0307
A	86%	88%	87%	96%
C (μm^4/cm)	0.0052	0.0056	0.0054	0.0061

Table 1: Thickness, refractive index (at λ=543.5 nm), A and C coefficients of the four tiles, as measured before the test.

In some runs a filter of D263 glass[1], 100 μm thick, was added on the back of the tiles in order to absorb photons above $\sim$3 eV which are most affected by Rayleigh scattering. In Figure 12 the transmission of the filter used is shown.

3 Simulation of the Test-Beam Setup

A detailed simulation program was developed using the GEANT4[6] software toolkit. This program configures the geometry of the experimental setup and simulates the various physics processes pertinent to the setup. In the simulation, a beam of charged pions going through the aerogel and the nitrogen produces Cherenkov photons with the corresponding Cherenkov angles along its trajectory.

[1]Thin glass D263 available from DESAG, D-31074 Grunenplan

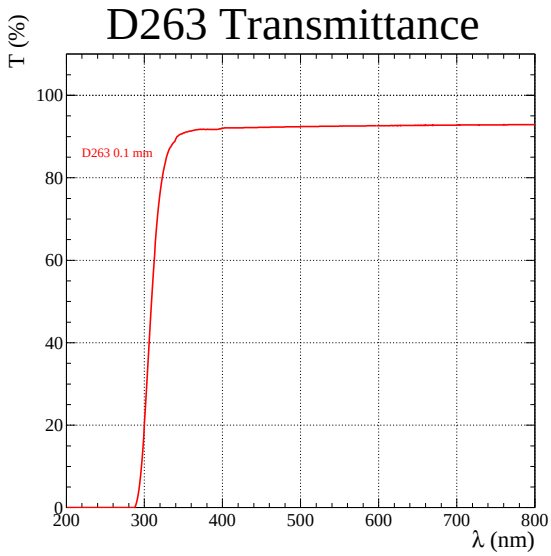

Figure 12: Transmission of the glass (D263) filter, 100 μm thick, as a function of the photon wavelength in nm.

3.1 Chromatic dispersion

Two parametrizations of the refractive index as a function of the photon wavelength are shown in Figure 13. The two n curves used in the simulation stem from two different approaches used for the extrapolation of the aerogel refractive index from normal SiO_2. In the first case the refractive index is parametrized as a function of the photon energy E by the Lorentz-Lorentz equation [7]:

$$n^2(E) = \frac{1 + 2cf(E)}{1 - 2cf(E)} \tag{2}$$

where

$$c = \frac{4\pi a \rho N_A}{2M} = 0.3738\ cm^3 \frac{\rho}{M} \tag{3}$$

$$f(E) = \frac{F_1}{G_1^2 - E^2} + \frac{F_2}{G_2^2 - E^2}. \tag{4}$$

and a is the Bohr radius, ρ is the density of the medium, N_A is the Avogadro number, M is the molecular weight, F_i and G_i are Sellmeier coefficients. Aerogel is approximated by fused quartz rescaled by the relative density. The curve is further scaled to match the measured refractive index of the aerogel sample at the wavelength λ=543.5 nm, for which a measurement is available.

The second method relies on considering the aerogel as a mixture of air and silica particles. According to the Clausius-Mossotti equation [9] for a binary mixture, and assuming $n = 1$ for the air:

$$n - 1 = \frac{3}{2}\frac{\rho}{\rho_s}\frac{(n^2{}_s - 1)}{(n^2{}_s + 2)} \quad (5)$$

where ρ and ρ_s are the densities of aerogel and solid silica respectively, and n_s is the refractive index of solid silica. The values of n_s are taken from an experimental data set of the refractive index of UV grade fused silica for λ between 180 and 900 nm [8]. This approach neglects, however, the presence of residues in the aerogel, such as water or ethanol and consequently underestimates $n_{aerogel}$ by roughly 10%. Therefore, the value of ρ is scaled upwards so that the calculated value of $n_{aerogel}$ at λ=543.5 nm matches the measured one. The assumption, here, is that the residues do not modify the shape of the dispersion curve.

The first parametrization is used as default in the simulation. The second has been used as comparison. Laboratory measurements on hydrofobic aerogel suggest that the Sellmeier parametrization is in good agreement with data [10].

3.2 Aerogel wall and optics

The photons incident on an optical boundary undergo reflection and refraction according to Fresnel equations [9]. The sides of the aerogel tiles and the filter are examples of the optical boundaries in this setup. Photons travelling in the aerogel undergo Rayleigh scattering [9] and absorption. The measured parameters of aerogel shown in Table 1 are used. The measured mirror reflectivity used is plotted in Figure 14.

At the HPD photo-cathodes, photo-electrons are created from photons according to the quantum efficiencies of the HPDs. The photo-electrons are assigned an energy corresponding to the electric potential between the cathode and the anode of the HPD and a direction defined by the cross focusing law, with a Gaussian spread (point spread function) which has a width of 50 microns at the anode.

The quantum efficiencies shown in Figure 5 are used for the evaluation of the expected photo-electron yield, with a 6% uncertainty on the measurements. The electrons backscattered at the silicon anode surface are assumed to be lost and contribute to the inefficiency in the hit detection. The overall efficiency of 82 % indicated in section 2.1 has been assumed.

4 Reference runs with Nitrogen as radiator

Three runs with N_2 as radiator were taken while focusing the mirror on a single HPD. The N_2 rings have an average radius of 1.75 mm on the anode and are completely contained in the chip as can be seen from Figure 15. Each run contains about ∼50000 events with ∼410000 hits.

Events with the N_2 radiator were simulated as described in Section 3. The refractive index for N_2 was calculated using a Sellmeier parametrization, with an average temperature of 20°C and a pressure of 968.5 mbar. The N_2 radiator length was measured to be 103 cm. In section 4.1 the analysis of photon yields is presented for the N_2 radiator. The comparison of the photon yields for data and simulation allows an extraction of the detection efficiency of the HPD. Sections 4.2 presents the analysis of the Cherenkov angle reconstruction for the N_2 radiator with two different methods. The first method uses a ray

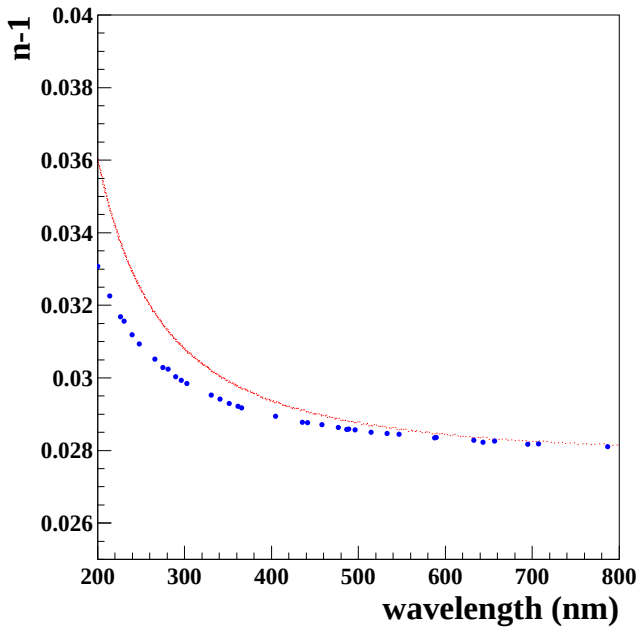

Figure 13: Refractive index of the aerogel as a function of the photon wavelength in nm. Red upper curve: parametrization with Sellmeier coefficients. Blue dots: parametrization based on the Clausius-Mossotti equation.

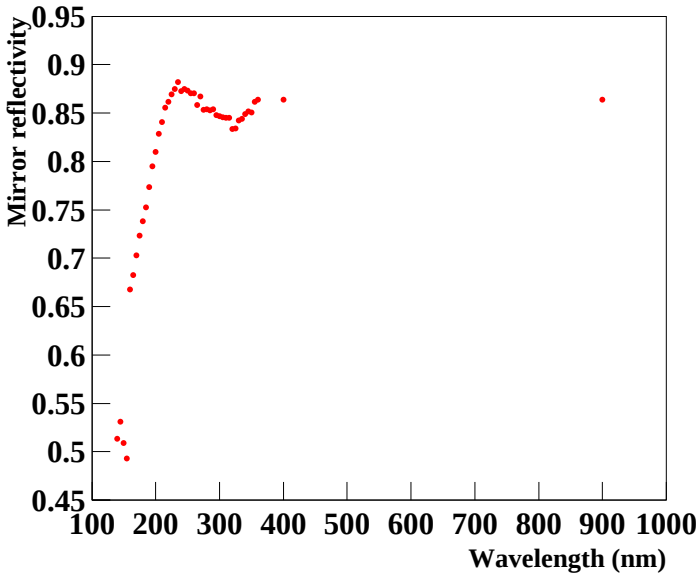

Figure 14: Reflectivity of the mirror as a function of the photon wavelength in nm.

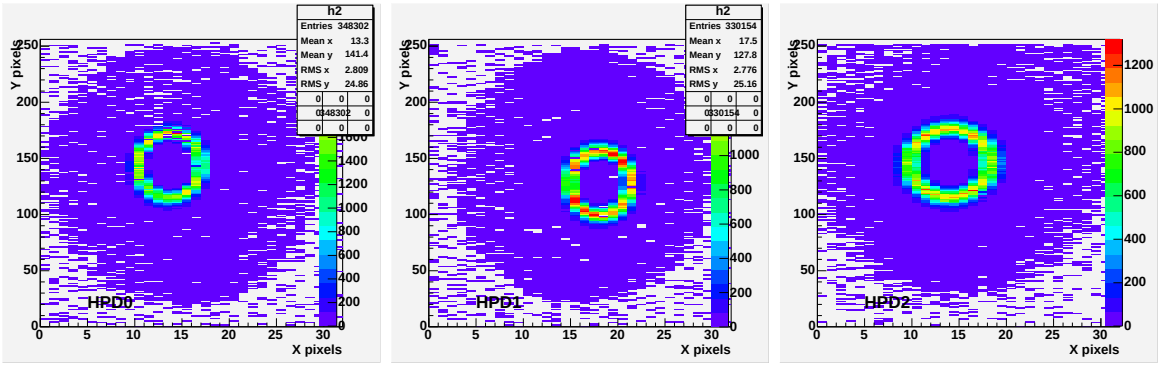

Figure 15: The pixel hit distributions for the data taken with the N_2 radiator.

tracing procedure while the second method is based on ring fitting. Comparison of both methods allows a better understanding of the different contributions to the systematic effects.

4.1 Photon Yield

The photon yield is defined as the average number of photo-electrons per event. Effects like ion feedback and charge sharing can increase the measured yield. Therefore the pixel hits are clustered, and each cluster is counted as one photo-electron.
When a photo-electron hits a residual gas molecule in the HPD vacuum envelope, a positively charged ion will drift back to the photo-cathode where it sets free many photo-electrons. This process, which is named ion feedback, will result in a large cluster structures ($\geq$ 10 pixels) on the anode. The fraction of ion feedback was found to be about 0.01% for HPD0 and HPD1 while it amounts to 0.07% for HPD2.
Charge sharing is responsible for a single photo-electron resulting in a double cluster. The fraction of double clusters observed in the data is shown in Table 2, distinguishing between horizontal, vertical and diagonal clusters. The difference between data and Monte Carlo comes from the fact that the Monte Carlo does not include charge sharing. The still large amounts of double clusters in the Monte Carlo samples are due to a geometrical effect. About 8 photo-electrons are expected to be distributed around the Cherenkov ring, hence it is very probable to have two or more photo-electrons hitting one pixel or for two photo-electrons to occupy adjacent pixels, which are then observed as one cluster. This effect is illustrated in Figure 16 where the number of clusters per event in Monte Carlo is plotted as a function of the number of generated hits per event. From these Monte Carlo events a probability matrix $P(j|N_{\text{clus}})$ was calculated, relating the probability to have j generated hits per event while N_{clus} clusters per event are measured. The following formula is then used to correct the measured number of clusters N_{clus} on an event by event basis:

$$N_{\text{clus}}^{\text{cor}} = \sum_j P(j|N_{\text{clus}})j. \tag{6}$$

For both data and simulation the Cherenkov angle is reconstructed with a ray-tracing procedure for every cluster, as described in detail in section 4.2. Clusters with a reconstructed Cherenkov angle inside a $\pm 3\sigma$ band around the mean Cherenkov angle are

	HPD0		HPD1		HPD2	
Double Clusters	N_2 data	MC	N_2 data	MC	N_2 data	MC
Total (%)	13.37 ±0.06	7.58 ± 0.07	17.6±0.07	6.74±0.07	13.8 ±0.06	7.56±0.07
Vertical (%)	9.68 ± 0.05	4.00 ± 0.05	13.8± 0.06	3.55±0.05	10.6±0.05	2.94±0.04
Horizontal(%)	1.65 ± 0.02	1.26 ± 0.02	2.1± 0.02	1.13±0.03	1.5± 0.02	1.66±0.03
Diagonal (%)	2.04 ± 0.02	2.29 ± 0.04	1.7± 0.02	2.06±0.04	1.7± 0.02	2.97±0.04

Table 2: The fraction of double clusters in the data compared to MC for the three HPDs.

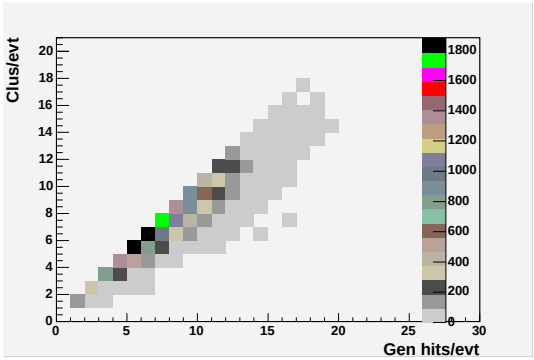

Figure 16: Number of clusters per event as a function of the number of generated hits

considered as signal, while cluster outside the 3σ band are considered as background. In the data 6.0%, 6.9% and 8.3% of the clusters are cut away, and 0.4%, 0.1% and 1.0% in Monte Carlo, for HPD0, HPD1 and HPD2 respectively. This background is due to ion feedback, reflections of the light at the silicon chip or in the quartz window etc., and is only partially included in the simulation. The amount of background under the signal peak was estimated from data runs. While the mirror was pointing at one HPD the two others were also read out. The hits seen in these HPDs are caused by stray light, electronic noise, ion feedback, etc. On average, in the signal region, $(3.6\pm 0.3)\times 10^{-3}$ hits per event were observed for HPD0, $(2.9\pm 0.2)\times 10^{-3}$ for HPD1 and $(2.9\pm 0.2)\times 10^{-3}$ for HPD2.

As can be seen from Figures 15 some HPDs have a few dead pixels. The fraction of dead pixels in the signal region is 2.2% for HPD0 and 1.2% for HPD1. No dead pixels were observed in the signal region for HPD2.

In order to obtain the final photo-electron yield, the number of clusters counted inside the $\pm 3\sigma$ region around the mean reconstructed Cherenkov angle is corrected on an event by event basis using equation (6) and a Poisson fit is performed. In the data the average number of background hits per event under the peak is then subtracted. In order to be compared to data, Monte Carlo yields are corrected for the fraction of dead pixels observed in the signal region. Results on the photo-electron yields are shown in Table 3. A systematic error on the Monte Carlo results is calculated from uncertainties on the quantum efficiency (6%), on the mirror reflectivity (2%) and on the value of the N_2 refractive index (2%). Additional systematic errors on both data and Monte Carlo results are due to the clustering corrections and to the background subtraction. They have been estimated from Monte Carlo to be 0.15, 0.13 and 0.06 hits per event on HPD0, HPD1

Pe Yield	HPD0	HPD1	HPD2
Data	7.07± 0.15	6.50±0.13	6.71±0.06
MC	7.12± 0.52	6.53±0.48	7.66±0.54
Data/MC	1.01± 0.08	1.00±0.07	0.88±0.06

Table 3: The photo-electron yields for the three HPDs as measured in data and Monte Carlo for the N_2 runs. Uncertainties are statistical and systematic.

and HPD2, respectively.

The ratio between the measured yield and the expected yield gives an indication of the HPD efficiency. In HPD0 and HPD1, data and Monte Carlo yields are compatible, confirming the value of the HPD efficiency of 82% used in Monte Carlo simulation (see section 2.1). For HPD2, the expectation is 12% higher than data, a reason can be the overestimation of the quantum efficiency used in the simulation.

As a cross check, the expected photo-electron yields have also been estimated from a direct calculation using the formula:

$$N = 2\pi\alpha LT \int R(\lambda)QE(\lambda)\frac{1}{\lambda^2}(1 - \frac{1}{(\beta n(\lambda))^2})d\lambda, \tag{7}$$

with L the radiator length of the medium (here 103 cm), T the transmission for N_2 (100%), β the velocity for 10 GeV/c pions. The average value of the refractive index over the whole wavelength range, assuming a temperature of 20°C and a pressure of 968.5 mbar, is 1.00028. Assuming 82% HPD efficiency, the calculated yields are 7.25 ± 0.51, 6.72 ± 0.47 and 8.36 ± 0.59 in HPD0, HPD1 and HPD2 respectively. Results are in good agreement with data, except for HPD2, as was also observed with the full Monte Carlo simulation.

4.2 Resolution on Cherenkov angle

The expected distributions of the Cherenkov angles of the *detected* photo-electrons, calculated for HPD0 and HPD1, are plotted in Fig. 17. They are determined from the index of refraction of the radiator, the particle speed and the detector spectral response. The dip in the curves is related to the dip in the quantum efficiency curves. The smaller angles correspond to longer wavelengths. The averages of the angular distributions (the expected Cherenkov angles) are shown in Table 4.

	$\theta(\pi)$ (mrad)	$\theta(e)$ (mrad)
HPD 0	19.3±0.7	23.8±0.7
HPD 1	19.4±0.6	23.9±0.4

Table 4: Expected average Cherenkov angles calculated considering the index of refraction of N_2, the quantum efficiency of the HPDs and 10 GeV/c pions and electrons.

Two different methods to reconstruct the Cherenkov angle were used. A ray-tracing procedure was used to reconstruct the Cherenkov angle for each recorded photo-electron. A second method determined the best fitted circle for each recorded event. The Cherenkov

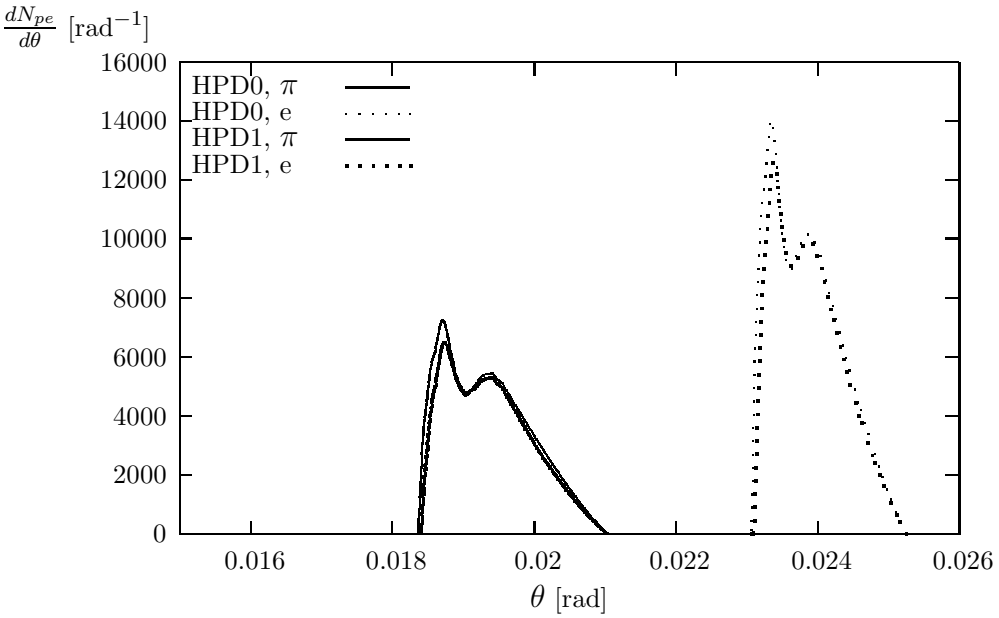

Figure 17: Distribution of the expected number of photo-electrons as a function of the angle of the originating Cherenkov photon. Curves were calculated for HPD0 and HPD1, for 10 GeV/c momentum pions and electrons, in the N_2 radiator.

angle was then derived from this radius. The analyses were performed both on data and on the Monte Carlo.

4.2.1 Ray-tracing method

The Cherenkov angle is reconstructed for each individual pixel cluster. An optical ray is traced from the middle point of the particle track in the radiator to the photo-electron emission point on the cathode. The Silicon beam telescope was inactive during the N_2 runs, hence no precise particle direction is known and it is assumed to be the nominal beam direction.

The distributions of the reconstructed angles are shown in Figures 18 and 19, fitted with a single Gaussian for Monte Carlo and a double Gaussian for data, to take into

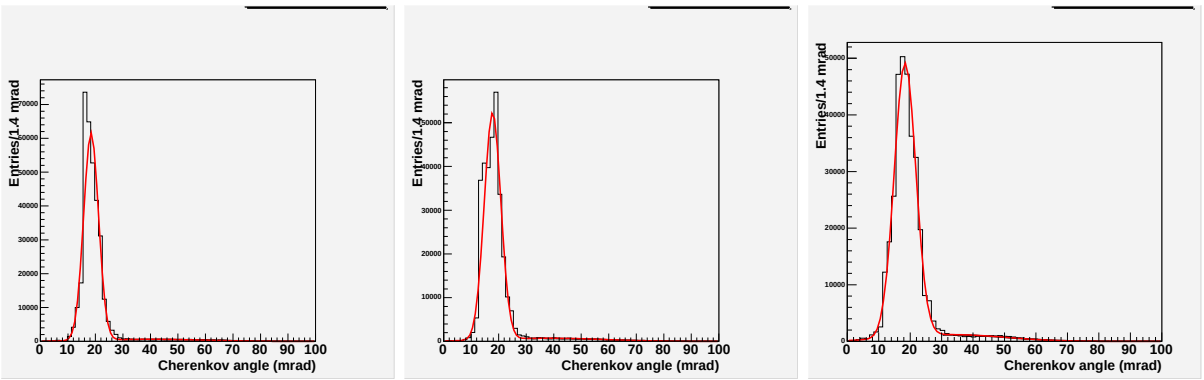

Figure 18: The reconstructed Cherenkov angle from N_2 data with a double Gaussian fit for the three HPDs.

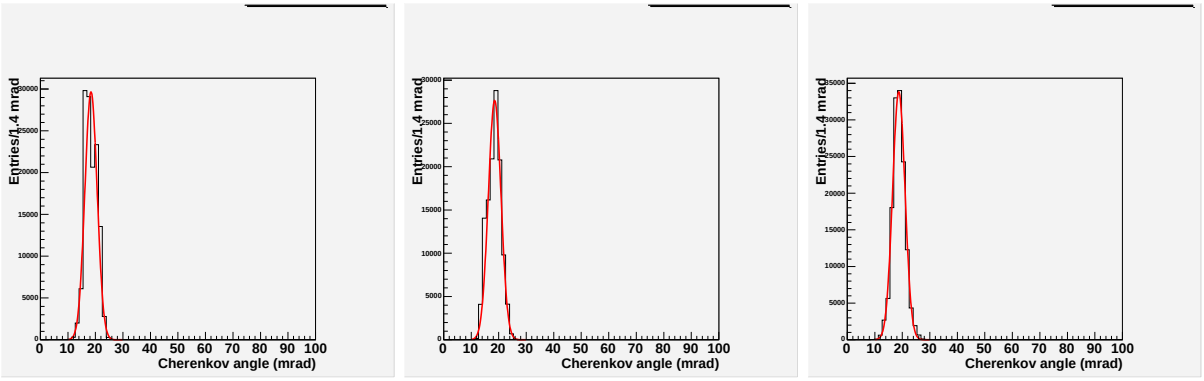

Figure 19: The reconstructed Cherenkov angle from Monte Carlo N_2 runs with the Gaussian fit for the three HPDs.

	HPD0		HPD1		HPD2	
	θ_C	σ_{θ_C}	θ_C	σ_{θ_C}	θ_C	σ_{θ_C}
Data (mrad)	18.4	2.7	17.8	3.0	18.4	3.4
MC (mrad)	18.8	2.2	18.8	2.3	19.0	2.4

Table 5: Reconstructed Cherenkov angles and resolutions for the ray-tracing method, on data and Monte Carlo.

account the background distribution as detailed in the following.
The average Cherenkov angles for data and Monte Carlo are given in Table 5 together with the sigmas of the fits that quantify the resolution on the Cherenkov angle. The statistical errors coming from the fit are of the order of 0.01 mrad. The Cherenkov angles reconstructed from data and Monte Carlo are in agreement as shown in Table 5. A discrepancy (∼1 mrad) is noted for HPD1 and could be ascribed to a difference in the radial demagnification curve of this device. No effect of refraction at the quartz entrance window was taken into account in the reconstruction of the Cherenkov angles. The bias ascribed to this effect is to lower θ_C about 0.5 mrad, for all HPDs. This value is determined comparing in the Monte Carlo the true photon emission angle with the one reconstructed from the true hit position on the photo-cathode including refraction, the true beam direction and the true emission point. Taking into account this bias the reconstructed Cherenkov angle values are in agreement with the expected angle of 19.3 mrad for all HPDs.

As it will be shown in 4.2.2, the beam contained a small fraction of electrons. The electron contamination enlarges the reconstructed Cherenkov angle distribution. A 5% fraction of electron events added in the Monte Carlo simulation increases the Cherenkov angle spread by 0.2 mrad, with respect to the case of pure pion beam. Table 5 has no electron events added.

The different systematic contributions to the resolution on the reconstructed Cherenkov angle as determined from the Monte Carlo, are given in Table 6. The main contributions come from the beam direction uncertainty and the pixelisation error. The contributions coming from the chromatic dispersion and the emission point error are less significant. The small differences between the totals in Table 6 with respect to the values

Contribution(mrad)	HPD0	HPD1	HPD2
Chromatic	0.7	0.7	0.7
Emission point	0.4	0.4	1.3
Pixel error	1.6	1.9	1.1
Beam direction	1.2	1.2	1.2
Total	2.2	2.4	2.2

Table 6: Contributions to the angular resolution as estimated from MC.

in Table 5 are due to the uncertainty in the fitting procedure. The total uncertainties are lower than those found in data. Part of this can be related to an underestimation of the point spread function. A specific simulation of the photo-electron trajectories inside the HPD indicates that the spread on the anode can be 160 μm, instead of the 50 μm assumed in the Monte Carlo. In this case an additional contribution of about 1.6 mrad has to be considered, giving a total resolution of about 2.8 mrad.

Some of the sources of background present in the data are: internal reflection of light inside the quartz window, dark counts, ion feedback. These background sources are not included in the Monte Carlo. Internal reflection of photons inside the quartz entrance window gives rise to secondary small peaks of pixel hits in the anode plane. This effect represents about 1.1 % (HPD0 and HPD1) and 1.6 % (HPD2) of the total signal hits. These peaks are spatially separated from the signal peak and do not influence the resolution of the Cherenkov angle.

4.2.2 Reconstruction with ring fitting

The data and Monte Carlo samples for HPD0 and HPD1 were also analyzed by fitting circles to the pixels hits on the anode plane on an event by event basis. The distribution of the pixel hits is not expected to be exactly circular, given that the rotational symmetry is broken by spherical aberration and by the lensing effect of the quartz window. With this method the effects coming from the beam divergence can be disentangled from other sources of uncertainty in the reconstruction. The fit was performed only to events with 4 or more hits. The uncertainty on the hit coordinate coming from pixelisation is taken into account, as well as its dependence on the azimuthal angle ϕ due to the different lengths of the pixel sides.

The distribution of the centers of the fitted circles is given in Fig. 20, for HPD0, in data. In the top-right frame of the figure the same distribution is shown after having applied a rotation of the axes. The frames on the bottom show the slices parallel to the rotated x-axis and to the rotated y-axis of the previous distribution, with Gaussian fits. The spread of the centers of the fitted circles in X and Y is mainly due to the beam divergence. The results for the data and for the Monte Carlo, averaged on HPD0 and HPD1, are shown in Table 7. The spreads determined in Monte Carlo are in partial agreement with the input values of the simulation (1.6 mrad in X and 0.7 mrad in Y) which corresponds to the beam divergence measured in data with the Silicon Telescope (see section 2.2). The uncertainties introduced by the fitting procedure could account for the difference. In data the different point spread function can be the reason for the additional spread. Fig. 21 and Fig. 22 show the distributions of the radii of the fitted

	$\sigma_{\theta,x}$	$\sigma_{\theta,y}$
Data (mrad)	2.5	2.0
Monte Carlo (mrad)	1.9	1.3

Table 7: Average beam divergence as derived from the spread of the distributions of the coordinates of the centers of the fitted circles.

	HPD0				HPD1			
	π		e		π		e	
	θ_C	σ_{θ_C}	θ_C	σ_{θ_C}	θ_C	σ_{θ_C}	θ_C	σ_{θ_C}
Data (mrad)	19.2	0.9 (2.6)	23.9	0.9 (2.6)	18.8	1.0 (2.9)	23.2	1.0 (2.9)
MC (mrad)	19.4	0.7 (2.0)	24.2	0.6 (1.7)	20.1	0.7 (2.0)	25.0	0.6 (1.7)

Table 8: Reconstructed Cherenkov angles and resolutions for the ring fitting methods, on data and Monte Carlo. In parenthesis the corresponding single photon resolutions.

circles for HPD0 and HPD1, for both data and Monte Carlo samples. One sigma cuts on the centers of the fitted circles were applied. The main peak can be associated with pion events, while the secondary peak shows the presence of electrons in the beam[2]. The algorithm was tested on the Monte Carlo and identified effectively the electron events when they were added to the simulation. The histograms are well fitted with double Gaussian functions.
The Cherenkov angles are calculated from the average radii. The results for the reconstructed angles and their resolution are summarized in Table 8. Also shown are the single photon resolutions evaluated multiplying by the square root of the average number of hits used in the fit (8.5 and 8.3 for HPD0 and HPD1, respectively). As this method can separate the electrons and pions in the beam, the Cherenkov angles for both contributions are listed. The Cherenkov angles measured in this way compare well with the expected ones listed in Table 4. A slightly smaller Cherenkov angle is observed for HPD1, as in the case of the ray-tracing algorithm.

As a conclusion, the Cherenkov angles reconstructed for data and Monte Carlo from the two methods are in agreement within errors, and also agree well with the expected ones. The angular resolutions also compare well, taking into account the average number of hits used in the circle fitting algorithm.

The differences between data and Monte Carlo simulation, due to a $\simeq$5% electron contamination of the beam and the point spread function, are not expected to give a measurable effect in the aerogel data, given the much larger Cherenkov angle.

5 Results with Aerogel

In Figure 23 the photo-electron hits on the silicon anode of the three HPDs for data and Monte Carlo are shown for a run with the aerogel and the filter. The measurement of the photo-electron yield and of the angular resolution for aerogel runs are described in the following sections.

[2]The relative abundance of the electrons can be determined from the data sample being $\sim$4.2 %.

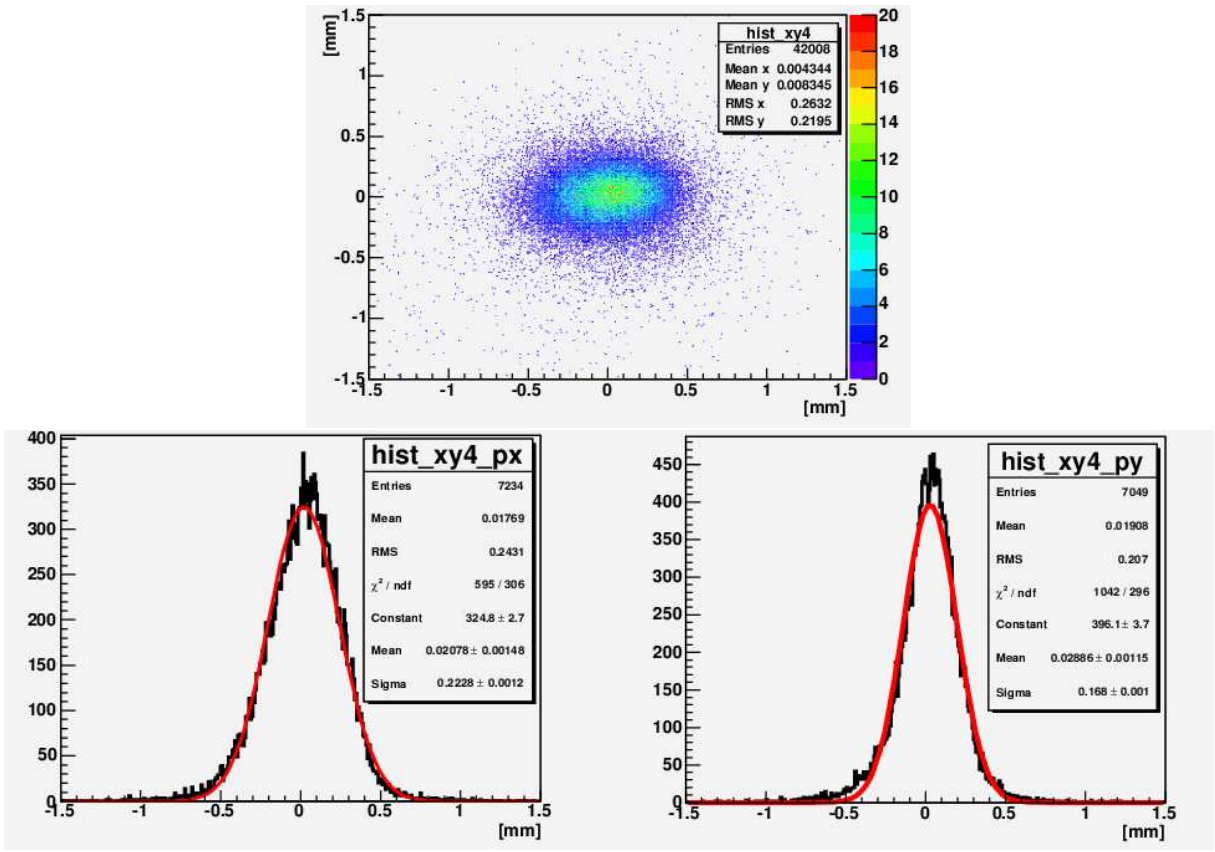

Figure 20: HPD0 N_2 data, centers of fitted circles. Top: the distribution of center coordinates (x_c, y_c). Bottom, left and right: x and y slices of the previous histogram crossing its center.

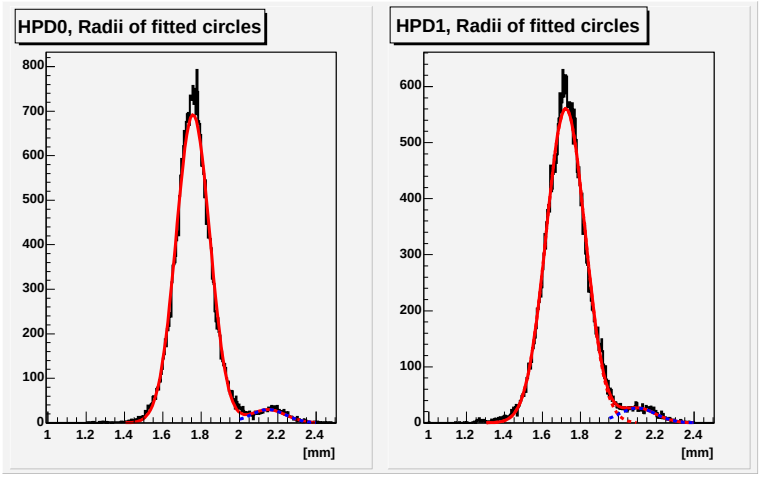

Figure 21: Distributions of the radii of the circles fitted to N_2 data runs. Left frame: HPD0. Right frame: HPD1. Double Gaussian fits are overlapped to the histograms. The secondary peak is due to electrons in the beam.

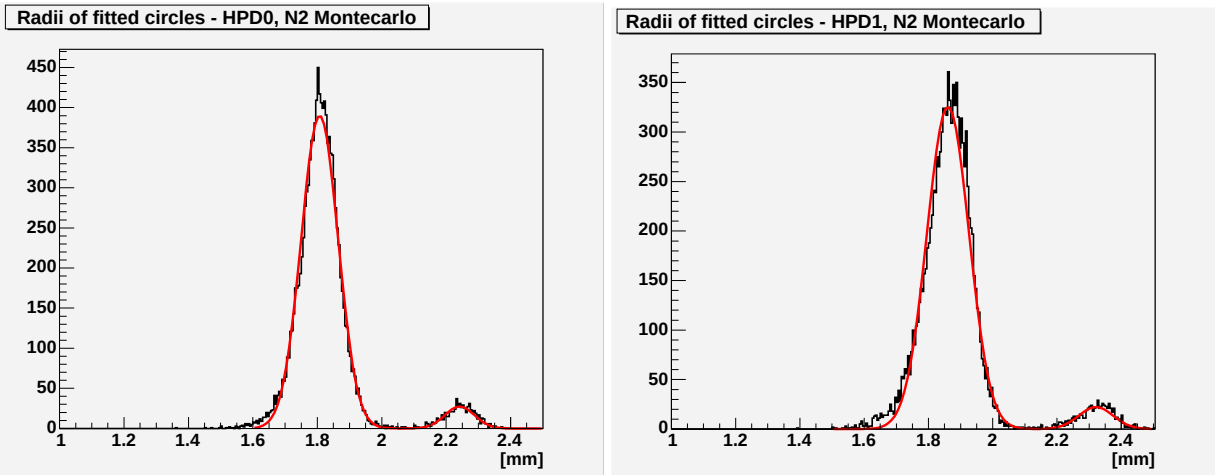

Figure 22: Distributions of the radii of the circles fitted to the Monte Carlo events for HPD0 (right) and HPD1 (left). Double Gaussian fits are overlapped to the histogram. Primary peak: 10 GeV/c pions. Secondary peak: 10 GeV/c electrons added to the beam in the simulation with 5% relative abundance.

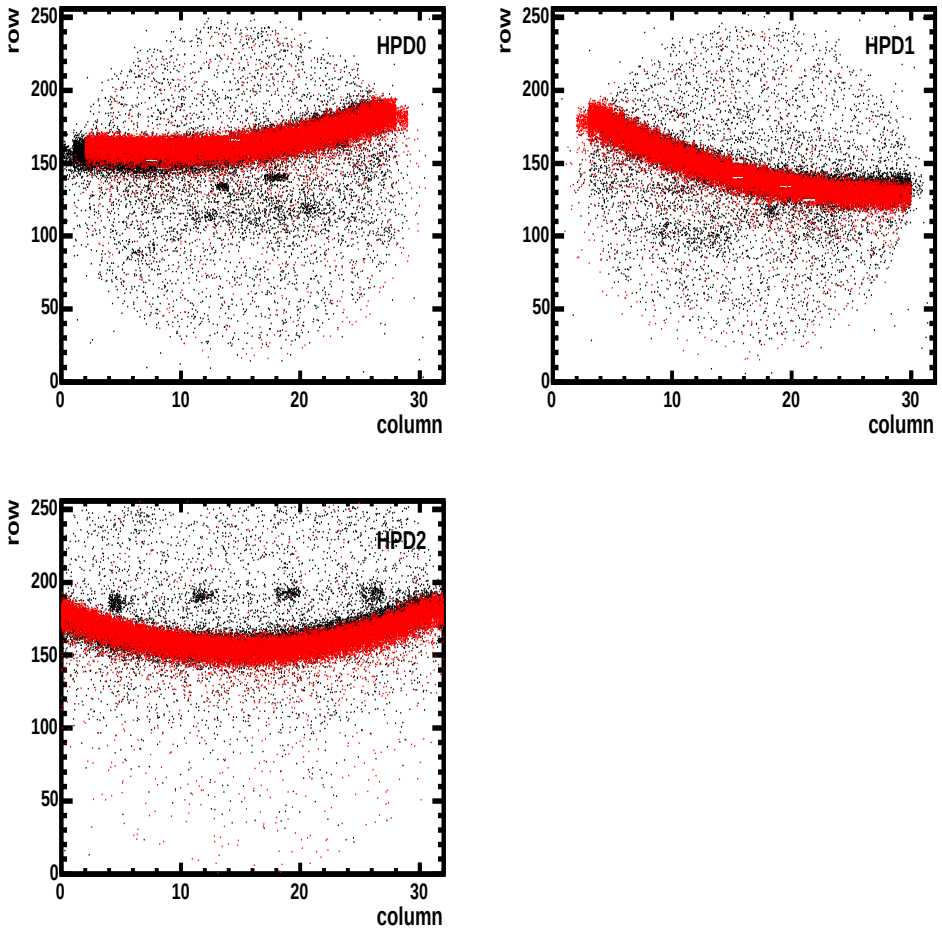

Figure 23: Hits on the silicon anode of HPD0, HPD1 and HPD2, respectively. Data are shown in black and the MC superimposed in red.

	With Filter			No Filter		
	HPD0	HPD1	HPD2	HPD0	HPD1	HPD2
Data	1.19±0.01	1.00±0.01	0.86± 0.01	1.60±0.01	1.41±0.01	1.21± 0.01
2π extrap.	11.7±0.2	9.3 ±0.2	9.1± 0.2	15.7±0.3	13.2 ±0.3	12.7± 0.3
MC	1.22±0.08	1.09±0.07	1.21± 0.08	1.62±0.10	1.47±0.09	1.59± 0.10
2π extrap.	12.0±0.7	10.2 ±0.7	12.7± 0.7	15.9±1.0	13.7 ±0.8	16.7± 1.1
Data/MC	0.98±0.06	0.92±0.06	0.71± 0.05	0.99±0.06	0.96±0.06	0.76± 0.05

Table 9: Number of photo-electrons per event per HPD in the signal region, as defined in the text. Errors on data are statistical, while those on Monte Carlo include the systematic uncertainties.

5.1 Photon Yield

The photo-electron yield is defined as the average number of photo-electrons detected per event. In each HPD a clustering procedure was applied as discussed in section 4.1. On average, 8.5%, 14.7% and 9.6% two-pixel clusters were found in HPD0, HPD1 and HPD2, respectively. Each cluster was considered as originating from one photo-electron. A possible underestimation of the number of photons due to the probability of two photo-electrons hitting neighboring pixels has been evaluated with the simulation and found to be of the order of 0.01 photo-electron per HPD, per event.

The spots seen in all HPDs (see Figure 23) are due to internal reflections off the back face of the HPD window. They are removed in data and in the corresponding pixels are masked in the Monte Carlo.

Background due to photo-cathode dark counts was studied by counting hits in special runs. In runs taken with triggering outside beam spills the average number of fired pixels per HPD per event has been found to be 2.2 x 10^{-3}. A run was also taken with a random trigger on the beam spill. The aerogel was in place but a black screen was placed at the exit window of it, preventing Cherenkov photons produced in the aerogel from reaching the mirror. In this case average number of fired pixels per HPD per event has been found to be 2.3 x 10^{-2}. This number, which includes the contribution of beam-related noise, has been subtracted from the number of photo-electrons in the analysis of the data.

A signal region is defined as a band $\pm 3\sigma_{\theta_C}$ around the average θ_C which is defined and reconstructed as described in section 5.2. The number of hits per event is counted in the band defined above.

The average number of photo-electrons per event is obtained from a Poisson fit to the distributions. The photo-electron yield for each HPD is given in Table 9 for runs with and without filter. The same procedure was applied to pixel hits obtained from the Monte Carlo simulation. Results are also shown in Table 9. Corrections for the effect of clustering and for missing pixels are included. The systematic uncertainty on the simulation is related to the values used for the mirror reflectivity (2%) and photo-cathode quantum efficiencies (6%).

Data and Monte Carlo agree reasonably for HPD0 and HPD1, while for HPD2 the simulation is above the observed signal. The same effect was observed for the N_2 rings (see section 4.1) and could be due to the assumed values of the photo-cathode quantum efficiency.

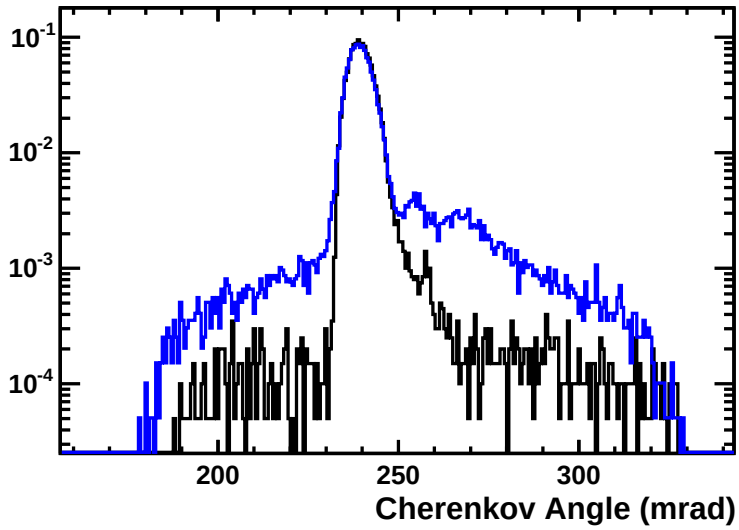

Figure 24: Cherenkov angle distributions normalized to the number of events in data (blue) and Monte Carlo (black).

From the simulation, the acceptance in ϕ with respect to a full ring is determined to be 0.102, 0.107 and 0.095 for HPD0, HPD1 and HPD2, respectively, with a relative uncertainty of 2%. Using these factors, the number of photo-electrons for a 2π ring, shown in Table 9, are calculated. The variations in photon yield among the three HPDs are mainly due to the different quantum efficiencies.

In Figure 24 the angular distribution of the detected photons in the data is shown, compared to Monte Carlo simulation. The number of photo-electrons falling outside the signal region is quite different in the Monte Carlo with respect to the data. Having subtracted background photons, hits outside the $3\sigma_{\theta_C}$ region are due to scattered Cherenkov photons. In the simulation the main contribution to scattering which has been considered is a series of several successive individual Rayleigh scatterings, which shows up as a flat distribution around the original direction of the Cherenkov photon.

Other effects, related to the HPD detectors, which could affect the data and were not simulated, include deviations of the photon trajectories due to internal reflections in the photo-cathode window, photo-electron reflections from the electrodes and from the anode silicon surface, and photo-electrons backscattering effects on the Si anode (see [11]). For the aerogel, an additional contribution could come from refractive index inhomogeneity of the tested tile.

A special study of the different components to the photo-electron yield was also done. Here an extrapolation from the region outside the signal band is used to estimate and remove the scattered contribution inside the signal band. A normalization function was first calculated using Monte Carlo to correct for the dependence of the HPD acceptance on the Cherenkov angle. In fact, due to the photo-cathode circular shape, a different number of pixels is seen for different Cherenkov angles, being higher for angles corresponding to rings crossing the center of the HPD. The correction function has been determined calculating, for the nominal beam direction, the number of pixels seen per Cherenkov angle and normalizing it to unity in the signal band. The normalized acceptance distributions

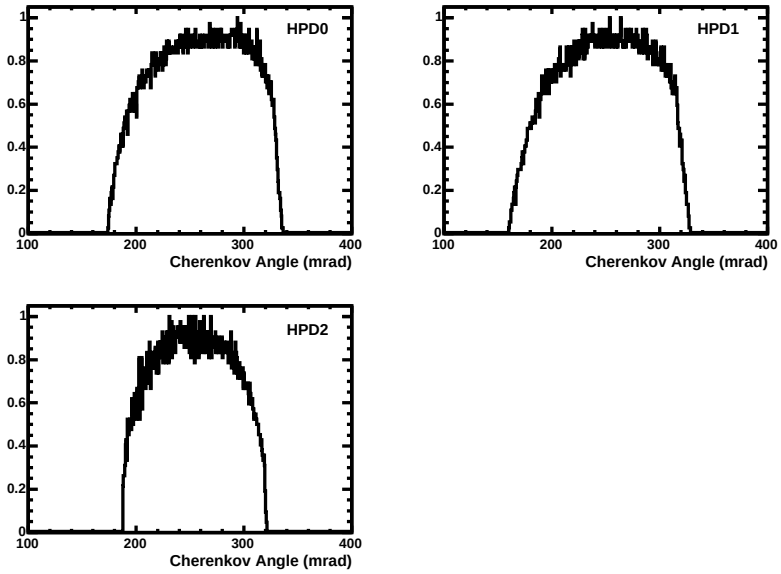

Figure 25: Normalized acceptance distributions as a function of Cherenkov angle in the three HPDs.

in the three HPDs are shown in Figure 25.

	With Filter			No Filter		
DATA	HPD 0	HPD 1	HPD 2	HPD 0	HPD 1	HPD 2
un-scattered	1.13±0.01	0.93±0.01	0.79±0.01	1.46±0.01	1.31±0.01	1.10±0.01
scattered	0.06±0.01	0.07±0.01	0.07±0.01	0.13±0.01	0.10±0.01	0.12±0.01
outside $3\sigma_\theta$	0.25±0.01	0.22±0.01	0.12±0.01	0.40±0.01	0.32±0.01	0.21±0.01
Monte Carlo	HPD 0	HPD 1	HPD 2	HPD 0	HPD 1	HPD 2
un-scattered	1.22±0.01	1.08±0.01	1.21±0.01	1.62±0.01	1.45±0.01	1.59±0.01
scattered	0.005±0.001	0.004±0.001	0.004±0.001	0.019±0.001	0.015±0.001	0.017±0.001
outside $3\sigma_\theta$	0.060±0.002	0.057±0.002	0.063±0.002	0.292±0.003	0.314±0.002	0.369±0.002

Table 10: Number of photo-electron per event per HPD in the 3σ band around the average Cherenkov angle and outside this region.

The corrected distribution of scattered photons is fitted in the region outside the $3\sigma_{\theta_C}$ band using a Gaussian function for data and a straight line for the simulation. The number of scattered photons in the signal band is calculated extrapolating these functions. It is then subtracted from the total number of photons in the signal band to obtain the number of un-scattered photons. Results are reported in Table 10.

5.2 Resolution on Cherenkov angle

A Cherenkov angle is reconstructed for all photo-electron hits with a ray-tracing procedure, using as particle direction the one determined with the three planes of the silicon telescope and assuming the emission point as midpoint in the aerogel. Due to chromatic

dispersion, the Cherenkov angle distributions are not expected to be perfectly Gaussian. However a fit to a single Gaussian was performed to get an indication of the average angle θ_C and the angular resolution σ_{θ_C} in each HPD. In Figures 26 and 27 the reconstructed Cherenkov emission angle is plotted in the three HPDs in the case where the filter is used and in the case where there is no filter. In Figure 28 the reconstructed Cherenkov emission angle is plotted in the simulation for the filter case.

The effect of refraction at the HPD quartz window has not been taken into account in the reconstruction of the photon direction. Truth information from the Monte Carlo simulation has shown that, as a result of this effect, a positive shift of the average Cherenkov angle of 1 mrad is seen in HPD2, which has a higher average angle of photon incidence than the other tubes. From here on results presented for data in HPD2 have been corrected a posteriori for this shift. No shift is seen for HPD0 and HPD1. Results for data and Monte Carlo are shown in Table 11.

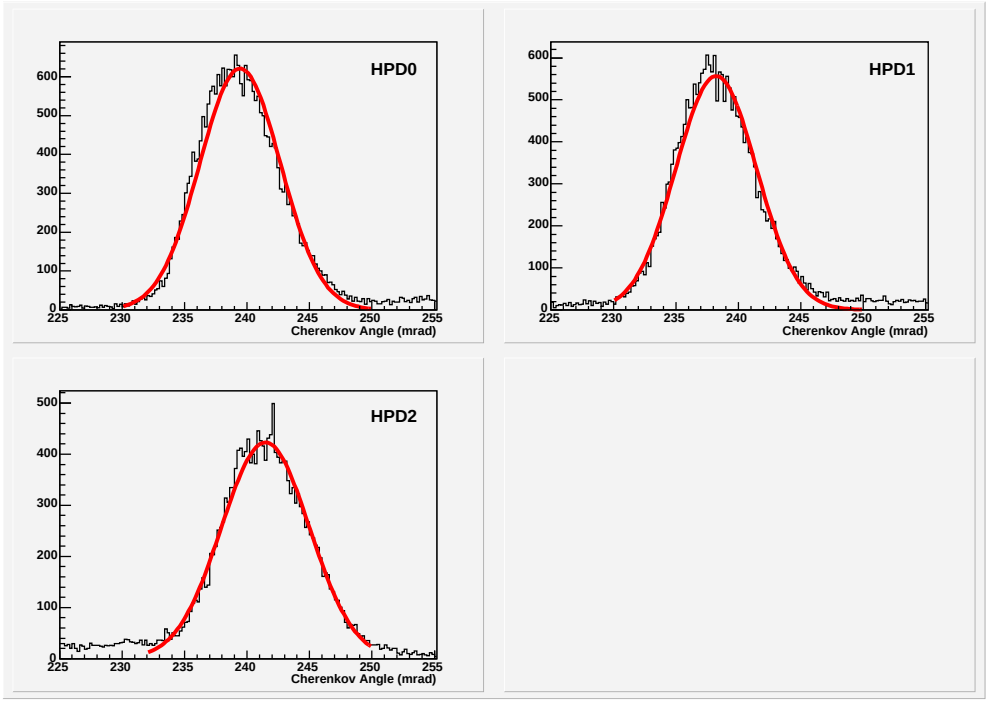

Figure 26: Reconstructed Cherenkov angle in the three HPDs. Superimposed a Gaussian fit. Run with filter.

The resolution in data is worse than in Monte Carlo. In order to better understand the different effects contributing to the final resolution, several studies have been performed using data and simulation.

The contribution of the chromatic dispersion in the aerogel to the angular resolution has been estimated with the simulation to be 2.3 mrad. The simulation uses the Sellmeier parametrization to model the aerogel refractive index. Using the Clausius-Mossotti parametrization shown in Figure 13, this contribution gives 1.7 mrad.

The tilting of the focusing mirror leads to a dependence of the image of a Cherenkov photon on its emission point along the track. However in the reconstruction the emission point is always taken as the midpoint of the aerogel; this introduces an error in the reconstructed Cherenkov angle. The contribution of this effect has been estimated from

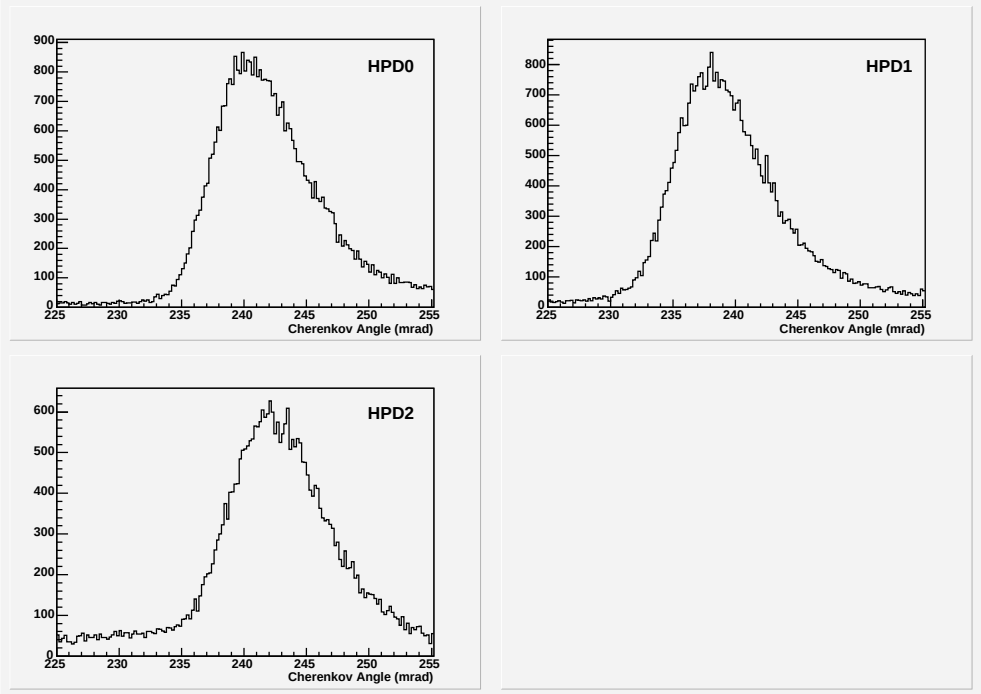

Figure 27: Reconstructed Cherenkov angle in the three HPDs. Run without filter.

		Data		Monte Carlo	
		θ_C	σ_{θ_C}	θ_C	σ_{θ_C}
Filter	HPD0	239.4	3.2	238.1	2.4
	HPD1	238.2	3.2	239.3	2.4
	HPD2	240.5	3.5	239.7	2.4
No Filter	HPD0	241.9	3.9	238.8	2.8
	HPD1	239.3	4.1	240.3	3.0
	HPD2	242.0	4.8	240.4	2.8

Table 11: Single photon resolutions in mrad for each individual HPD.

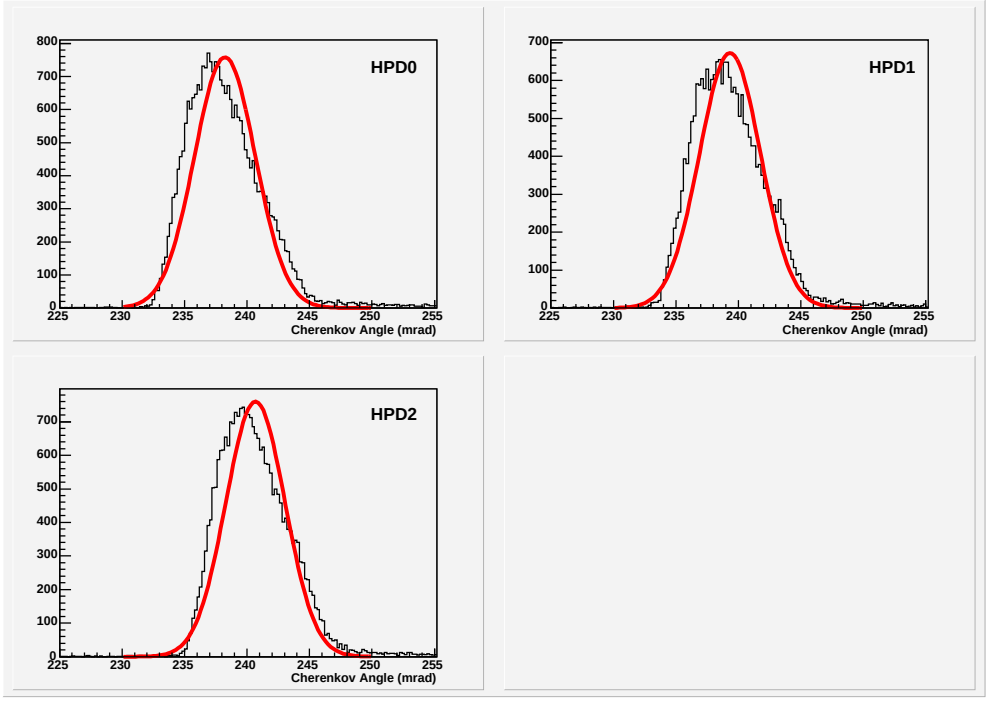

Figure 28: Reconstructed Cherenkov angle in the three HPDs in Monte Carlo simulation. Superimposed a Gaussian fit. Run with filter.

the simulation to be about 0.7 mrad, by comparing results with the true photon emission point and results obtained with the center of the aerogel tile.

Another contribution to the Cherenkov angle resolution is the finite pixel size. This has been studied in the simulation by comparing the Cherenkov angle reconstructed with the true photo-electron origin and the pixel coordinates and was found to be about 0.5 mrad, with a small variation among the HPDs due to the different orientation of the pixels with respect to the Cherenkov ring. This also includes the contribution of the point spread function.

The contribution related to the uncertainty in the beam direction is negligible, as the event by event beam direction was measured using the silicon telescope. The contribution from the pixelization of the silicon sensors is about 0.05 mrad. Fully neglecting the beam divergence, i.e. not using the silicon telescope information, would cause an increase in the resolution of 1.5 mrad in HPD0 and HPD1 and 0.8 mrad in HPD2, to be added in quadrature.

The effect on the angular resolution of the uncertainties in the value of the HPD quantum efficiencies used in the simulation has been found to be negligible.

A summary of the different contributions to the angular resolution obtained in the Monte Carlo simulation is shown in Table 12. For runs without filter the chromatic contribution increases to about 2.7 mrad, while the other contributions are almost unchanged.

Another contribution to the angular spread in the data can come from the residual misalignment in the reconstruction. For a perfectly aligned system the angular resolution is expected to be inversely proportional to the square root of the number of photo-electrons. A mean Cherenkov angle has been calculated per event, excluding clusters falling outside the 3 σ_θ signal region, and the distribution fitted with a Gaussian, in the same manner

	With Filter	No Filter
Chromatic	2.3	2.7
Emission point	0.7	0.7
Pixel	0.5	0.5
Quartz window refraction	0.15	0.2
Sum	2.5	2.8

Table 12: Breakdown of different contributions to the angular resolution in Monte Carlo, in the filter and no filter case. Values are in mrad, averages on the three HPDs.

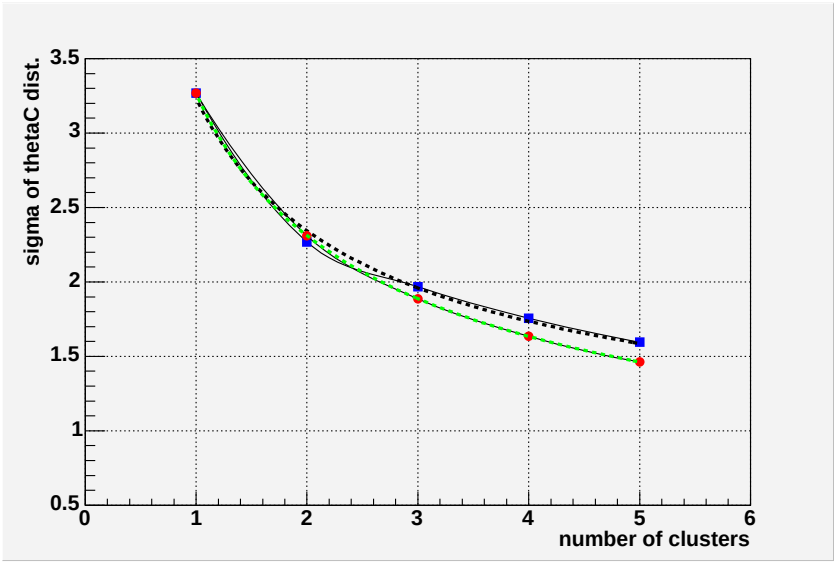

Figure 29: Cherenkov angle resolution as a function of the number of photo-electrons (blue squares) and expected dependence normalized to the single hit result (red circles).

as for the single photon fit. The resolution, as a function of the number of clusters used, is shown in Figure 29. A fit to the data gives: $\sigma^2_{fit} = (3.17)^2/N_{clus} + (0.73)^2$, indicating a contribution from residual misalignment of the order of 0.7 mrad.

The linear demagnification law shown in Figure 6 has been used to reconstruct the data. A check was performed to understand the effect of possible distortions in the electric field or inaccuracies in the demagnification law used. The resolution has been determined in the data using, in each HPD, only the central region of the ring, containing about 18% of the events, as shown in Figure 30. A reduction in the resolution of about 0.3 mrad has been observed for each HPD, giving a $\simeq$ 1.2 mrad contribution in quadrature.

An additional contribution to the resolution observed in the data, not included in the simulation, is related to possible dis-uniformity of the refractive index of the aerogel tile. For this tile a spread $\sigma(n-1)/(n-1) = 1.0\%$ was measured in [12] which would correspond to a 1.1 mrad spread in the Cherenkov angle.

The sum of all these additional effects leads to an angular resolution of about 3.1 mrad and can partially explain what has been observed in data.

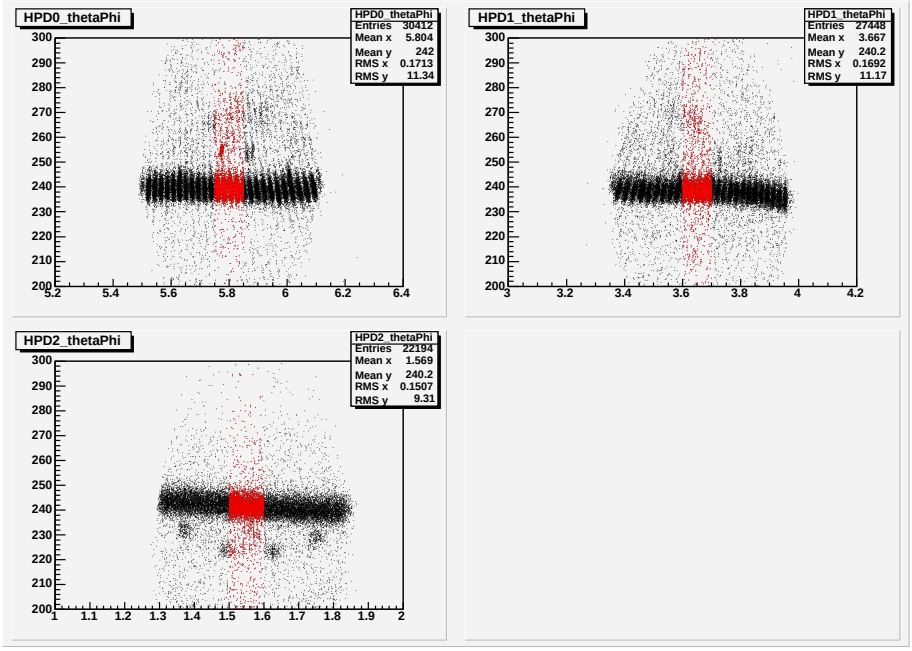

Figure 30: Cherenkov angle versus ϕ angle along the ring, for the three HPDs. In red the regions selected for the test. The ϕ angle is defined with respect to a spherical coordinate system with origin in the center of the three HPDs system.

.

HV	20kV		18kV		16kV		14kV	
	θ_C	σ_{θ_C}	θ_C	σ_{θ_C}	θ_C	σ_{θ_C}	θ_C	σ_{θ_C}
HPD0	239.2	4.0	241.9	3.9	238.3	4.0	237.8	4.1
HPD1	239.0	4.1	239.3	4.1	239.1	4.1	240.0	4.1
HPD2	240.8	5.0	243.0	4.8	241.1	5.2	241.1	5.1

Table 13: Single photon resolutions in mrad for the three HPDs, as a function of the applied high-voltage. Values are in mrad. All runs are with aerogel without filter.

5.3 Photon yield and angular resolution as a function of High-Voltage

Data were collected with different settings of the high voltage supplied to the HPD detectors, ranging from 14 kV to 20 kV. The voltage used for standard runs was 18 kV. The dependence of the photo-electron yield on the high-voltage is shown in Figure 31. A progressive increase is found. Results on the Cherenkov resolution as a function of the high-voltage are shown in Table 13. The values listed are for a single Gaussian fit, in a range of 200 to 280 mrad. The results show a stable response of the HPD devices with respect to the voltage supply.

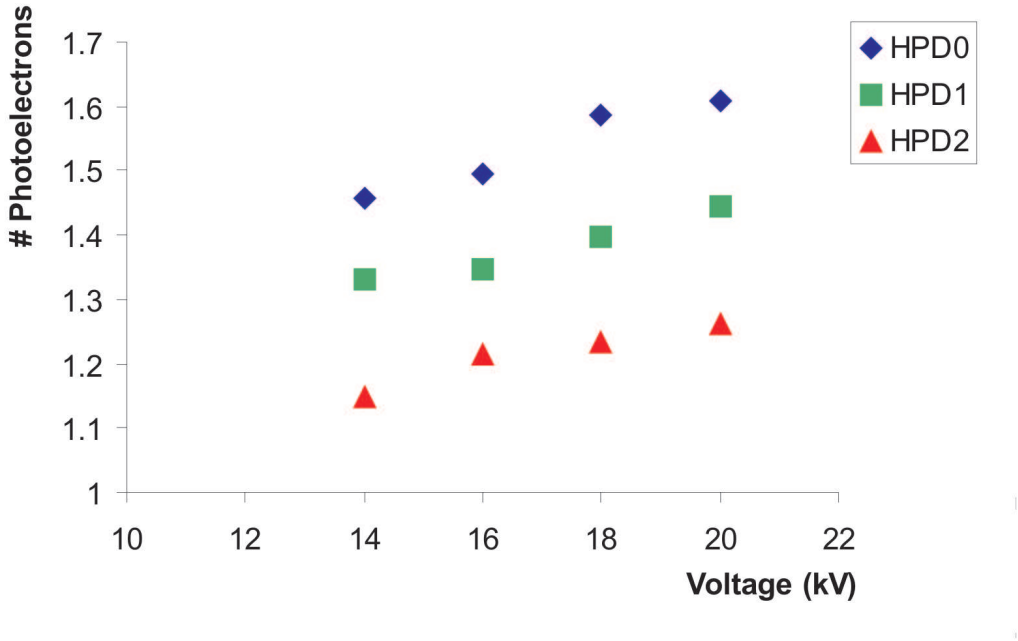

Figure 31: Photo-electron yield in the three HPDs as a function of the high-voltage supply.

5.4 Effect of filter

The effect of the 100 μm thick filter on the photon yield is a decrease of 26%, 26%, 29% in data and 25%, 26%, 23% in the Monte Carlo, in HPD0,HPD1,HPD2 respectively. The difference for HPD2 between data and Monte Carlo can be related to an overestimation of the QE used in the simulation, in the region below 300 nm. The effect on the Cherenkov angle distribution is shown in Figure 32 for data and Monte Carlo.

The distribution in the no filter case is highly asymmetric. The results of Gaussian fits change from about 3.2 mrad to about 4.3 mrad. Taking into account the total number of photo-electron available to the ring reconstruction, the angular resolution improves with the filter by about 10%.

In the Monte Carlo simulation the filter thickness was increased from 100 μm to 300 μm. Correspondingly the angular resolution improves by about 0.5 mrad, while the number of photo-electrons in the 3 σ_θ signal region decreases by about 4.%.

5.5 Proton/pion separation

The beam used in this test can be chosen to contain a mixture of pions and protons of momentum 10 GeV/c. Only runs with no filter were taken in this study. Figure 33 shows the two Cherenkov rings in the HPDs. A fit to the reconstructed Cherenkov distribution with two Gaussians gives θ_π=238.0 mrad and θ_p=221.4 mrad with a single photon resolution of about 5 mrad. The measured resolution is degraded in this case by the superposition of the two rings generated by pions and protons travelling along the same direction. Using the measured distance between the two peaks and the single photon resolution measured in the previous section in the filter case, the pion/proton separation significance at 10 GeV/c is $(5.2\sqrt{N})\sigma$, where N is the average number of detected photo-electrons.

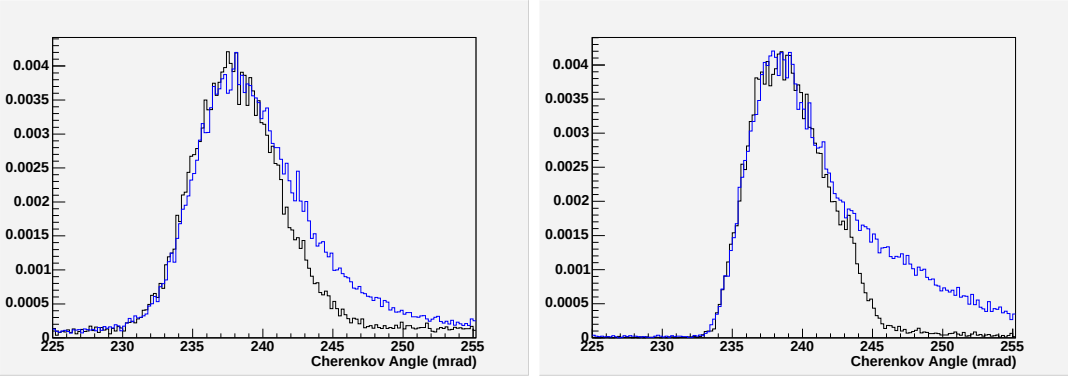

Figure 32: Reconstructed Cherenkov angle in data (left) and Monte Carlo (right) in HPD0. The case where the filter is in place is shown in black, and the case where the filter is removed is shown in blue. The distributions are normalized to the height of the peak in each case.

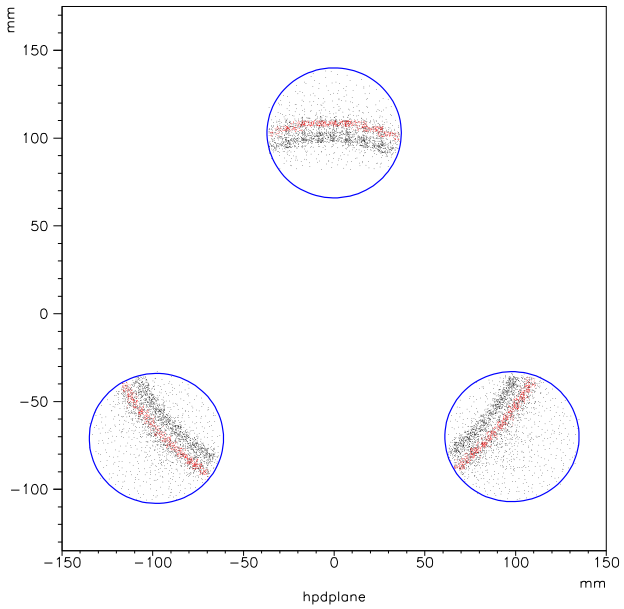

Figure 33: Cherenkov rings measured by the three HPDs for a run without filter with a beam composed of pions and protons of 10 GeV/c. In red, hits falling in a ± 2 mrad band around the expected Cherenkov ring produced by pions are shown.

.

5.6 Scan across aerogel tiles

In the LHCb detector [13], the aerogel radiator will consist of several tiles. It is therefore important to understand what is the effect of the tile surfaces on the photon yield and the Cherenkov angle resolution. All data considered in the previous sections were taken with the beam centered in the middle of one aerogel tile (tile number 1 in Table 1). Other runs have been taken moving laterally the aerogel wall inside the vessel or moving the vessel itself perpendicular to the beam, in the horizontal and in the vertical directions, in order to scan different regions of the tile close to the borders. Steps of 5 mm have been taken across the borders. In the horizontal plane the beam profile at the aerogel entrance was Gaussian with a R.M.S. of about 2.5 mm, therefore all intermediate positions have been covered. The silicon telescope planes have been used to determine the incoming particle position on an event by event basis. All runs were taken without filter at the aerogel exit. The number of hits in each HPD has been measured, summing over the whole HPD, as a function of the particle entrance point in the aerogel. Figure 34 shows results for the horizontal scan across the vertical tile border. A loss of photons is observed when the Cherenkov light is passing through the tile border. The loss is different in HPD2 with respect to HPD0 and HPD1 because the parts of ring seen by the detectors are differently affected by crossing the tile borders. In the simulation the photons incident on the tile boundary undergo internal reflection and refraction according to the Fresnel equations [9]. A gap of 0.1 mm between the tiles has been considered. The predictions of the simulation are also shown in Figure 34.

For this comparison the efficiency in HPD2 has been scaled by a factor 0.80 in the simulation, according to the results of sections 4.1 and 5.1. The agreement with the data is satisfactory, taking into account the imperfect modelling of the beam focusing.

It must be stressed that these data were taken with particle directions almost parallel to the tile lateral surfaces, while the angular incidence in the aerogel detector in LHCb will be of several degrees, hence improving the overall transmission.

6 Conclusions

The test-beam run performed at CERN in October 2003 with a RICH prototype and three pixel HPDs was successful and the results have been analyzed in various respects. The performance of the HPDs was excellent; from these studies we have learned that complete information and careful monitoring of a few experimental parameters is extremely important, i.e. :

- geometrical alignment of the HPDs,
- photo-cathode quantum efficiency of each device,
- demagnification function,
- value of the point spread function.

The possibility to measure the particle direction on an event by event basis is also important for the understanding of the angular resolution.

The photon yield measured for both Nitrogen and Aerogel radiators result in agreement with expectations. The Cherenkov angle resolution for Nitrogen rings is almost compatible

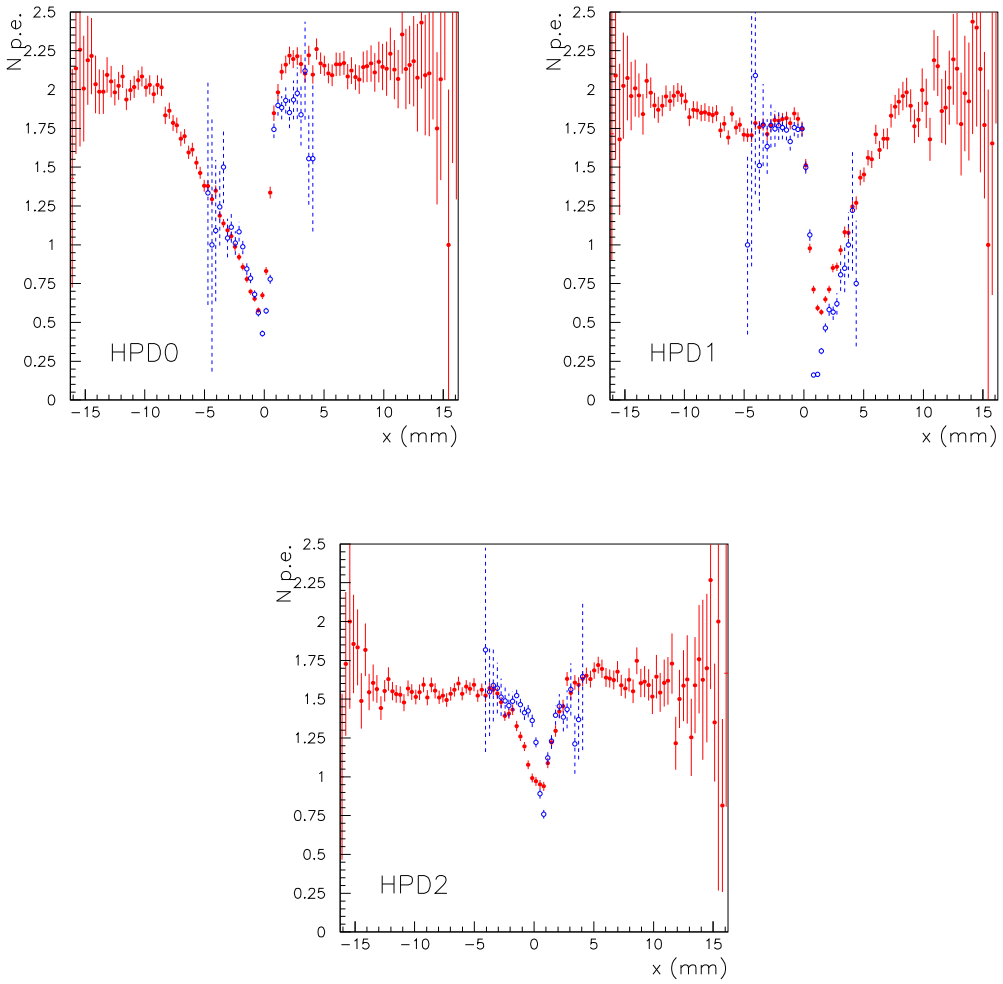

Figure 34: Number of hits per event per HPD as a function of the particle entrance point in the aerogel tile, across the border between two tiles. Red, full circles: data, blue, empty circles: simulation. The data are taken without filter.

.

with expectations. A degraded resolution is found in the Aerogel data with respect to the Monte Carlo and several possible reasons have been considered. The photon yield and angular resolution are adequate for LHCb preformance.

References

[1] T. Gys, *et al.*, Nucl. Instr. and Meth. A 449 (2000) 48.
T. Gys, T *et al.*, Nucl. Instr. and Meth. A 465 (2001) 240.
K. A. George, *et al.*, Nucl. Instr. and Meth. A 504 (2003) 286.

[2] K. Wyllie, *et al.*, Nucl. Instr. and Meth. A 530 (2004) 82.

[3] M. Moritz, IEEE Trans. on Nucl. Sci., NS-51 (3) (2004) 1060-1066.

[4] A.F.Danilyuk, *et al.*, Nucl. Instr. and Meth. A 433 (1999) 406.

[5] A.J.Hunt *et al.*, Mater.Res. Soc. Symp. Proc (1984) 275.

[6] GEANT4 - A Simulation Toolkit, S.Agostinelli *et al.*, Nucl. Instr. and Meth. A506(2003) 250-303.

[7] See T.Ypsilantis and J.Seguinot, Nucl. Instr. and Meth. A 343(1994) 30.

[8] Melles Griot Optics Guide.

[9] Classical Electrodynamics, J.D. Jackson, John Wiley & Sons Inc. NewYork, 1975. ISBN 0-471-43132-X.

[10] M. F. Villoro *et al.*, Nucl. Instr. and Meth. A480(2002) 456-462.

[11] N. Kanaya *et al.*, Nucl. Instr. and Meth. A 553(2005) 41-45.

[12] D.Perego, 2004 IEEE Nuclear Science Symposium, Medical Imaging Conference, Roma, October 16-22, 2004

[13] LHCb Reoptimized Detector Design and Performance, CERN/LHCC 2003-030, LHCb TDR 9, 9 Sep 2003.